

# Variational operator learning: A unified paradigm marrying training neural operators and solving partial differential equations

Tengfei Xu<sup>1</sup>, Dachuan Liu<sup>1</sup>, Peng Hao <sup>\*1</sup>, and Bo Wang<sup>1</sup>

<sup>1</sup>State Key Laboratory of Structural Analysis, Optimization and CAE Software for Industrial Equipment, Department of Engineering Mechanics, Dalian University of Technology, Dalian 116024, China

## Abstract

Neural operators as novel neural architectures for fast approximating solution operators of partial differential equations (PDEs), have shown considerable promise for future scientific computing. However, the mainstream of training neural operators is still data-driven, which needs an expensive ground-truth dataset from various sources (e.g., solving PDEs' samples with the conventional solvers, real-world experiments) in addition to training stage costs. From a computational perspective, marrying operator learning and specific domain knowledge to solve PDEs is an essential step for data-efficient and low-carbon learning. We propose a novel data-efficient paradigm that provides a unified framework of training neural operators and solving PDEs with the domain knowledge related to the variational form, which we refer to as the variational operator learning (VOL). We develop Ritz and Galerkin approach with finite element discretization for VOL to achieve matrix-free approximation of system functional and residual. We then propose direct minimization and iterative update as two possible optimization strategies. Various types of experiments based on reasonable benchmarks about variable heat source, Darcy flow, and variable stiffness elasticity are conducted to demonstrate the effectiveness of VOL. With a label-free training set and a 5-label-only shift set, VOL learns solution operators with its test errors decreasing in a power law with respect to the amount of unlabeled data. To the best of the authors' knowledge, this is the first study that integrates the perspectives of the weak form and efficient iterative methods for solving sparse linear systems into the end-to-end operator learning task.

## 1 Introduction

Solving partial differential equations (PDEs) has widespread applications in science and engineering. Conventional solvers based on a variety of classical numerical approaches (e.g., finite element methods (FEMs), finite volume methods (FVMs), finite difference methods (FDMs), meshfree methods) have been developed and achieve great achievements in the last decades, and they can give solutions that meet engineering accuracy requirements under appropriate settings. Commercial software developed on the basis of these conventional solvers has been used extensively in engineering. However, the conventional solvers cannot learn knowledge or experience from their history of solving previous problems, which means they have to solve a new problem from scratch each time, even if it is highly similar to the ones they have solved before. The limitation leads to heavy computational costs in scenarios that require multiple simulations of different parameters, such as inverse problems, optimum design and uncertainty quantification. With the current rapid development of deep learning algorithms, software and hardware, training neural networks to learn

---

\*Corresponding author: haopeng@dlut.edu.cn

the solution *operators* [32, 29, 28, 19, 42, 11, 10, 21, 15, 48] becomes a promising way to break through the above limitation of the conventional solver. But the training process of neural networks requires often a number of labels from simulation or experiments as ground truth data, which can be scarce and expensive to obtain. Many attempts [7, 44, 37, 24, 41, 9, 38, 50, 31, 11, 39] (see Table 1) to embed domain knowledge like physical laws and principles into neural networks have been made to make the training process label-efficient and even label-free. Like the classical numerical approaches that solve PDEs with different forms, these techniques also deal with different forms of PDEs: the differential form (the strong form), the equivalent integral form, the variational form (the weak form) and the minimization form (see Table 1). The weak form transforms differential equations into integral equations, reducing the difficulty of solving by lowering the order of PDEs. Compared to the strong form, the weak form reduces the continuity requirements of the solution, which is less strict and more robust, making it appropriate for describing many of the real-world phenomena with non-smooth and even discontinuous physics. Besides, many powerful classical numerical approaches, especially FEMs and FVMs, are based on the weak form, which have developed mature mechanisms for handling boundary conditions and determining convergence of solutions. Embedding the weak form with these well-developed mechanisms in deep neural networks can help us overcome some of the difficulties like boundary condition management [46] encountered in the strong form embedding. Moreover, the classical Ritz method and Galerkin method based on the weak form transform the original PDEs problem into solving a sparse linear system, which a lot of iterative techniques [40] can be applied to solve with low costs. We provide Table 1, where we list of some of the representative existing literature of solving and learning PDEs, from classical approaches to some recent work combining machine learning. From Table 1, we observe three such combinations, which are physics-informed DeepONet (PI-DeepONet) [50], physics-informed neural operator (PINO) [31] and physics-informed variational DeepONet (V-DeepONet) [11]. However, both PI-DeepONet and PINO are mostly based on the strong form. V-DeepONet, like the deep Ritz method [7] and the literature [41], chooses to set the system functional as the loss function, which is based on the minimization form. Combining operator learning model and the specific domain knowledge, especially the weak form, is worth exploring and will lead us to new numerical approaches suitable for solving parameterized PDEs.

**Our contributions.** In this Article, we propose the variational operator learning (VOL), a novel paradigm that combines training neural operators and solving partial differential equations with the variational form. To the best of the authors’ knowledge, this is the first study that integrates the perspectives of the weak form and efficient iterative methods for solving sparse linear systems into the end-to-end operator learning task. The proposed VOL trains neural operators with a label-free training set. The distribution-shift operation with a 5-label-only shift set (see section 5), which also exists in the conventional data-driven paradigm in the previous work [28], is the only part requiring labels in the VOL algorithm. The main contributions of this work are summarized as follows:

- Based on the idea of Ritz method and Galerkin method, we propose Ritz approach and Galerkin approach respectively in the framework of VOL. These two approaches can approximate system functional and system residual with FEM discretization in a matrix-free manner.
- We introduce direct minimization and iterative update as two optimization strategies into the framework of VOL to minimize the residual norm. Specifically, for iterative update strategy, we integrate steepest decent method (SD) and conjugate gradient method (CG) into VOL with an efficient restart-update manner.
- We investigate VOL with various experimental results. Our scaling experiments show the proposed VOL can learn operators and solve the PDEs effectively across different benchmarks given enough

label-free data. We also conduct resolution experiments, comparative experiments verifying generalization benefits of VOL, and comparative experiments for different optimization strategies.

## 2 Related work

**Surrogate modeling.** Surrogate modeling has been proposed to alleviate the computational burden of conventional solvers. Two main strategies, reduced order modeling methods (ROMs) and data-fit modeling methods (DFMs), have been adopted in the surrogate modeling. The main idea of these strategies is to seek a surrogate model of the original complex model so as to reduce or avoid the use of the conventional solver at the evaluation stage. ROMs [17] use limited available snapshots from the original high-fidelity computational models to build simplified ones in the space of reduced basis. The constructed reduced-order models are computationally efficient compared with original full-order models. On the other hand, DFMs [8] including response surface methods, Kriging methods and neural networks, perform interpolation or regression of parameter-response pairs sampled from the high-fidelity dataset. The popular deep learning approach can also be considered as a kind of DFMs. An enormous amount of work of deep neural networks, including the neural operators [35, 20, 9, 29, 28, 32], has focused on utilizing deep learning techniques to design excellent neural surrogate models.

Two stages are usually required for both ROMs and DFMs to get a surrogate model in a purely data-driven manner:

(1) *Data preparation.* At this stage, high-fidelity labels from the simulation of the conventional solvers or real-world experiments are produced and collected. Both ROMs and DFMs require often a fair number of such expensive labels.

(2) *Model construction (model training).* Available labeled data from stage (1) are utilized to construct the surrogate model, which brings another computational cost.

It is worth noting that, despite the existence of techniques such as active learning [43] that tightly couple these two stages, they are in reality isolated from each other. From a model perspective, the data preparation stage just provides limited labels as examples, and keeps itself a black box to the surrogate models to be trained in the whole process of simulating or experimenting. Besides, from a solver perspective, the model training stage has no influence on the solving process in the data preparation stage, for example, it cannot accelerate the convergence of solving. Models trained in such a purely data-driven fashion can only acquire knowledge indirectly through the labels. If the model can learn directly from the domain knowledge, it is possible to skip the data preparation stage, and the model training process is to a certain extent equivalent to solve the original PDEs. Two ways to help coupling the model with domain knowledge, i.e., domain knowledge embedding and deep model embedding, are discussed in the next paragraph.

**Domain knowledge embedding and deep model embedding.** Domain knowledge embedding is to embed domain knowledge (e.g., governing equations, discretization schemes, symmetries, variational principles) into the architecture of the (deep learning) model and the training process. We have listed some of the representative domain knowledge embedding methods in Table 1. Broadly speaking, domain knowledge embedding methods can either be mesh-free [7, 44, 37, 24, 41, 50, 11] or mesh-based [9, 38, 31]. In the mesh-free framework, residual of certain forms of PDEs is computed at some sampled positions in the solution domain, where the residual computation is heavily relied on automatic differentiation with the neural ansatz. On the other hand, in the mesh-based framework, the residual is computed with a certain discretization scheme, e.g., FDMs [9], FVMs [38]. We introduce them with some representative work:

(1) *Mesh-free framework with automatic differentiation.* Automatic differentiation is a powerful tool to calculate derivatives in deep learning. The derivatives of the output with respect to input parameters such as spatial coordinates and time, the Jacobian matrix, and even the Hessian matrix can be easily obtained with

automatic differentiation. Thus, the governing equations also their weak forms with derivative terms can be implemented elegantly in deep learning. Here we list some representative research that uses automatic differentiation to implement domain knowledge embedding. Deep Ritz method [7] constructs a functional with automatic differentiation approximating derivatives of the trial function, and numerical integration, which sets the minimization objective as the functional. Deep Galerkin method (DGM) [44] and physics-informed neural network (PINN) [37] are very similar, both of which use the residual error of the strong form as part of the loss function, deriving the residual term with automatic differentiation. Besides, both of them also treat the boundary conditions as penalty terms. PI-DeepONet [50] also calculates derivatives in loss function with automatic differentiation. Note that treating the strong form residual as a loss function can be viewed as embedding an equivalent integral form obtained through the collocation method with the delta function as the test function in the loss function. However, we have not classified it as an equivalent integral form in Table 1 for the sake of clarity.

(2) *Mesh-based framework with a certain discretization scheme.* Discretization technique, on the other hand, computes the derivatives and the residual of PDEs with various discretization schemes. Tricks about convolution filters have been adopted to represent various discretization schemes. Motivated by the domain knowledge of the multigrid algorithm, a deep neural architecture called MgNet [16] is designed and successfully used in dataset CIFAR-10 and CIFAR-100 [26] for image classification. The following Meta-MgNet [5] use convolutions to represent discrete forms of differential operators, providing improved smoothers for the multi-grid algorithm. FEA-Net [52] uses convolution kernel to express stiffness feature of the structure discretized by finite elements. PhyGeoNet [9] and DiscretizationNet [38] discretize the output of the deep learning model with the finite difference discretization scheme and finite volume discretization scheme respectively to approximate the derivative terms and the residual in the governing equations. The proposed VOL in this Article chooses FEMs as the discretization scheme. For VOL, we design Ritz approach and Galerkin approach (see section 5.1) to form the global algebraic equation system in FEMs and calculate the residual in a matrix-free manner. Compared the mesh-free framework, Galerkin approach in VOL derives residual with no automatic differentiation, which is more resource-efficient in terms of computation and video memory. Compared with existing domain knowledge embedding work that also utilizes FEMs as the discretization scheme, for example, Meta-MgNet [5], which reduces its Q1-element implementation to FDM, FEA-Net [52], which derives its convolution kernel analytically, VOL considers standard isoparametric elements. Moreover, VOL is allowed to perform Gauss quadrature of arbitrary order and shape function of arbitrary order, which is more practical and closer to actual engineering.

In contrast to domain knowledge embedding, deep model embedding is to embed the deep learning model in the classical numerical approach to enhance the capabilities of the classical numerical approaches. Deep potential [14] leverages deep neural network representation of the potential energy surface for atoms and molecules system, which is a promising alternative to the classical potential representation in molecular dynamics and Monte Carlo simulations. Problem-independent machine learning [18] embeds a simple feedforward neural network in the framework of extended multi-scale finite element method [54] to learn the mapping between discretized material density field of the coarse element and the multi-scale numerical shape functions of the element. Deep conjugate direction method [22] uses the output of a deep convolutional neural network embedded in the algorithm to construct a good search direction which accelerates the convergence for solving large, sparse, symmetric, positive-definite linear systems. Fourier neural solver [6] embeds a neural network in the stationary iterative method to help to eliminate error components in frequency space.

For both approaches, we just list some of the representative research in recent years. It is also noted that these two approaches are not mutually exclusive, instead, they are complementary to each other, which means a method can be both domain knowledge embedding and deep model embedding, and we can use either one or both of them to solve the problem.

**Operator learning and neural operators.** Operator learning is to let the model learn the operator between two function spaces. Operator learning models, which we say are *operator-based*, can give prediction over a whole parameter set of parameterized PDEs. In Table 1, we classify some of the representative existing methods according to whether they are function-based or operator-based. Neural operators refer to specific neural network architectures designed for operator learning. According to the type of input and output of the neural networks, the existing architectures of neural operators can be divided into two categories:

(1) *Point-wise*. Inspired by the universal approximation theorem for operators [3, 4], deep operator network (DeepONet) [32], as a representative architecture of this category, receives the parameter field and a query point, and then output solution of the query points in the computational domain, which has a branch net for encoding discrete function space and a trunk net for encoding the coordinate information of query points, and the output of which is the inner product of the output of two nets. Following work based on DeepONet includes learning multiple-input operators [21], combing DeepONet with physics-informed machine learning [50], replacing the trunk net with basis functions precomputed by proper orthogonal decomposition [33]. Recently, a general neural operator transformer (GNOT) [15] is proposed, with a heterogeneous normalized attention layer design, and GNOT is also designed to handle multiple input functions and irregular meshes.

(2) *Field-wise*. These architectures [29, 28, 53, 48] input discrete parameter fields and output discrete solution fields. Fourier neural operators (FNO) [28] parameterize the integral kernel in the Fourier space and utilize the idea of shortcut connection, producing a powerful Fourier layer. The implicit Fourier neural operator (IFNO) [9] utilizes the Fourier layer in an implicit manner, which lets the data flow pass through the Fourier layer recurrently and has better training stability. Factorized Fourier neural operator (F-FNO) [48] adopts Fourier factorization and a handful of other techniques about network design and training settings to enhance the model performance. In this Article, we focus on training the field-wise neural operators due to the natural similarity between field-wise output and mesh settings in FEMs.

It is worth noting that, in addition to these neural operators specifically designed for operator learning, the idea of operator learning has also been combined with various neural architectures and approaches, including convolutional neural networks [35] and the generative neural networks [20], principal component analysis [1, 27], meta-learning [19], transfer learning [10], attention mechanism [25, 15], manifold learning [42].

### 3 Preliminaries

#### 3.1 Forms of partial differential equations

Consider  $\Omega \subseteq \mathbb{R}^d$ , where  $d$  is a fixed number in  $\mathbb{N}^+$ .  $\mathcal{S}$  denotes the boundary of  $\Omega$ . Without loss of generality, we start with the strong form of the stationary PDEs:

$$\begin{aligned} \mathbf{A}(\mathbf{u}(\mathbf{x})) &= 0, \mathbf{x} \in \Omega \\ \mathbf{BC}(\mathbf{u}(\mathbf{x})) &= 0, \mathbf{x} \in \mathcal{S} \end{aligned} \quad (1)$$

Multiply Eq. 1 by an arbitrary test function  $\mathbf{v} \in \mathcal{C}_c^\infty(\Omega)$ , we get the weighted integral form or equivalent integral form of PDEs

$$\int_{\Omega} \mathbf{v}^T \mathbf{A}(\mathbf{u}) d\Omega + \int_{\mathcal{S}} \mathbf{v}^T \mathbf{BC}(\mathbf{u}) d\mathcal{S} \equiv 0. \quad (2)$$

Then, with integration by parts lowering the order of variables, we can get the weak form of PDEs

$$\int_{\Omega} \mathbf{C}(\mathbf{v})^T \mathbf{D}(\mathbf{u}) d\Omega + \int_{\mathcal{S}} \mathbf{E}(\mathbf{v})^T \mathbf{F}(\mathbf{u}) d\mathcal{S} \equiv 0. \quad (3)$$

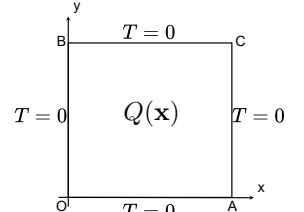
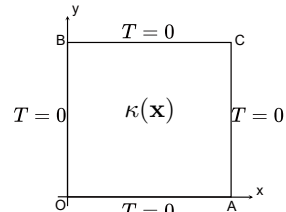
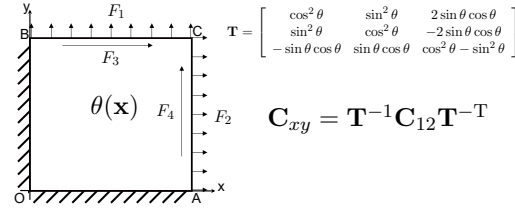
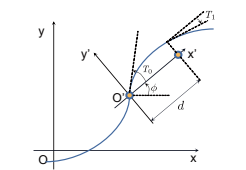
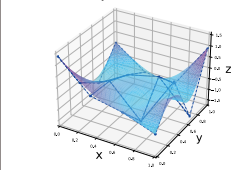
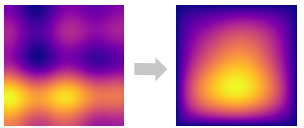
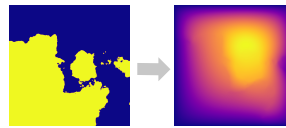
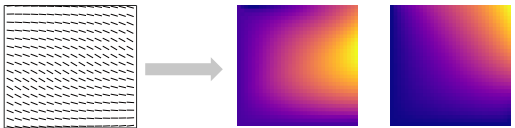
Problem	<p>Variable heat source</p> 	<p>Darcy flow with variable conductivity</p> 	<p>Variable stiffness elasticity</p> 
Governing PDEs	$\begin{cases} -\nabla \cdot (\kappa \nabla T) = Q & \text{in } \Omega, \\ T = \bar{T} & \text{on } \mathcal{S}_D, \\ (\kappa \nabla T) \cdot \mathbf{n} = \bar{q} & \text{on } \mathcal{S}_N, \\ (\kappa \nabla T) \cdot \mathbf{n} = \bar{h}(T_\infty - T) & \text{on } \mathcal{S}_R, \end{cases}$		<p>Equilibrium equations</p> $\begin{cases} \sigma_{ij,j} + f_i = 0, & \text{in } \Omega \\ \bar{X}_i = \sigma_{ij} n_j, & \text{on } \mathcal{S}_\sigma \\ u_i = \bar{u}_i, & \text{on } \mathcal{S}_u. \end{cases}$ <p>Geometric equations</p> $\varepsilon_{ij} = \frac{1}{2}(u_{i,j} + u_{j,i})$ <p>Physical equations</p> $\boldsymbol{\sigma} = \mathbf{C}\boldsymbol{\varepsilon}$
Modeling strategy	<p>Random source term:</p> $Q(\mathbf{x}) \sim \mathcal{GP}(0, k_l(\mathbf{x}, \mathbf{x}')) \text{ W/m}^2$ $k_l(\mathbf{x}, \mathbf{x}') = \sigma e^{-\frac{\ \mathbf{x}-\mathbf{x}'\ ^2}{2l^2}} \text{ W/m}^2$ <p>where <math>l = \frac{1}{2}, \sigma = 1</math></p>	<p>Random conductivity:</p> $\eta \sim \mathcal{N}(0, (-\Delta + 9I)^{-2})$ $\kappa(\mathbf{x}) = \begin{cases} 12 & \text{if } \eta(\mathbf{x}) \geq 0 \\ 3 & \text{if } \eta(\mathbf{x}) < 0 \end{cases}$	<p><b>A</b> Linear 1-D variation</p>  $\theta(x') = \phi + (T_1 - T_0) \frac{ x' }{d} + T_0$ <p><math>(\phi, T_0, T_1)</math> are sampled from <math>(-\frac{\pi}{2}, \frac{\pi}{2})^3</math> with LHS</p> <p><b>B</b> B-Splines surface</p>  $\theta(x, y) = Z(x, y) = \sum_{i=0}^n \sum_{j=0}^m N_{i,p}(u) N_{j,q}(v) Z_{i,j}$ <p><math>Z_{i,j}</math> are sampled from <math>(-\frac{\pi}{2}, \frac{\pi}{2})^{(m+1) \times (n+1)}</math> with LHS</p>
Learning goal	<p>Learn <math>\mathcal{N}_\theta : Q \mapsto T</math></p> 	<p>Learn <math>\mathcal{N}_\theta : \kappa \mapsto T</math></p> 	<p>Learn <math>\mathcal{N}_\theta : \theta \mapsto \mathbf{u}</math></p> 

Figure 1: A schematic representation of the VOL benchmarks in this work.

	Function-based			Operator-based				Type of methods				Form of PDEs			
	✓	✓	✓	✓	✓	✓	✓	Classical numerical approach	Data-driven modeling	Domain knowledge embedding	Differential form	Equivalent integral form	Minimization form	Variational form	
Analytical methods	✓	✓	✓	✓	✓	✓	✓				✓				
FDMs	✓	✓	✓	✓	✓	✓	✓				✓				
Weighted residual methods	✓	✓	✓	✓	✓	✓	✓							✓	
Ritz method	✓	✓	✓	✓	✓	✓	✓							✓	
Galerkin method	✓	✓	✓	✓	✓	✓	✓							✓	
FEMs	✓	✓	✓	✓	✓	✓	✓							✓	
FVMs	✓	✓	✓	✓	✓	✓	✓							✓	
ROMs	✓	✓	✓	✓	✓	✓	✓							✓	
Deep Ritz method [7]	✓	✓	✓	✓	✓	✓	✓		✓			✓			
DGM [44]	✓	✓	✓	✓	✓	✓	✓		✓						
PINN [37]	✓	✓	✓	✓	✓	✓	✓		✓						
VarNet [24]	✓	✓	✓	✓	✓	✓	✓		✓					✓	
Literature [41]	✓	✓	✓	✓	✓	✓	✓		✓						
PhyGeoNet [9]	✓	✓	✓	✓	✓	✓	✓		✓					✓	
DiscretizationNet [38]	✓	✓	✓	✓	✓	✓	✓		✓						
DeepONet [32]	✓	✓	✓	✓	✓	✓	✓		✓						
FNO [28]	✓	✓	✓	✓	✓	✓	✓		✓						
PI-DeepONet [50]	✓	✓	✓	✓	✓	✓	✓		✓				✓		
PINO [31]	✓	✓	✓	✓	✓	✓	✓		✓				✓		
V-DeepONet [11]	✓	✓	✓	✓	✓	✓	✓		✓				✓		
<b>VOL (ours)</b>	✓	✓	✓	✓	✓	✓	✓		✓					✓	

Table 1: Summary of some of the representative existing methods of solving and learning PDEs.

And note the weak form can be expressed in such an abstract form

$$\text{Find } \mathbf{u} \in V, \text{ such that } a(\mathbf{u}, \mathbf{v}) = L(\mathbf{v}), \quad (4)$$

When  $a(\mathbf{u}, \mathbf{v})$  is symmetric, we can also write the minimization form of the PDEs. By treating the test function  $\mathbf{v}$  as the variation of  $\mathbf{u}$ , we can derive the functional  $\Pi$  of the system from the weak form. In this case, the original problem (solving PDEs) has been transformed into a functional minimization problem

$$\Pi = \Pi(\mathbf{u}) \rightarrow \min_{\mathbf{u}} \Pi(\mathbf{u}). \quad (5)$$

Note  $\Pi$  can also be written in such an abstract form

$$\Pi = \frac{1}{2}a(\mathbf{u}, \mathbf{u}) - L(\mathbf{u}). \quad (6)$$

The solutions to Eq. 3, Eq. 4 and Eq. 5, Eq. 6 are called *weak solutions*. Eq. 5 and Eq. 6 are also called "weak form" sometimes, but to emphasize the Eq. 5 and Eq. 6 minimize the system functional, while the weak form provides a more general approach, we call them minimization form in this Article.

### 3.2 Ritz method and Galerkin method

Ritz method and Galerkin method are two representative ways of utilizing the weak form and minimization form to solve PDEs. They both approximate weak solutions in finite-dimensional spaces. We introduce these two methods with stationary problems of PDEs in Hilbert spaces.

- *Ritz method*

Ritz method focuses on minimizing functional in Eq. 5 and Eq. 6 of the system. Choose  $V_n$  a finite dimensional subspace of  $V$ ,  $\dim(V_n) = n$ , and then construct a basis  $(\phi_1, \dots, \phi_n)$  of  $V_n$ . Then,  $\mathbf{u}$  can be approximated with the  $\mathbf{u}^n$  uniquely decomposed on the basis

$$\mathbf{u}^n = \sum_{j=1}^n u_j \phi_j. \quad (7)$$

Then,  $\Pi$  can be written as

$$\begin{aligned} \Pi(\mathbf{u}^n) &= \frac{1}{2}a(\mathbf{u}^n, \mathbf{u}^n) - L(\mathbf{u}^n) \\ &= \frac{1}{2}a\left(\sum_{j=1}^n u_j \phi_j, \sum_{i=1}^n u_i \phi_i\right) - L\left(\sum_{i=1}^n u_i \phi_i\right) \\ &= \frac{1}{2} \sum_{i=1}^n \sum_{j=1}^n a(u_j \phi_j, u_i \phi_i) - \sum_{i=1}^n L(u_i \phi_i) \\ &= \frac{1}{2} \sum_{i=1}^n \sum_{j=1}^n u_j u_i a(\phi_j, \phi_i) - \sum_{i=1}^n u_i L(\phi_i). \end{aligned} \quad (8)$$

Thus,  $\Pi$  can be rewritten under algebraic form

$$\Pi = \frac{1}{2} \mathbf{u}^T \mathbf{A} \mathbf{u} - \mathbf{u}^T \mathbf{b}, \quad (9)$$



where  $A_{ij} = a(\phi_j, \phi_i)$ ,  $b_i = L(\phi_i)$ . To minimize  $\Pi$ , Ritz method lets the gradient of the function  $\Pi(u_1, \dots, u_n)$  be a zero vector

$$\frac{\partial \Pi}{\partial \mathbf{u}} = \mathbf{A}\mathbf{u} - \mathbf{b} = \mathbf{0}. \quad (10)$$

- *Galerkin method*

Galerkin method is based on the weak form of PDEs. Like Ritz method, Galerkin method also uses the basis  $(\phi_1, \dots, \phi_n)$  of  $V_n$  to construct approximation of  $\mathbf{u}$ . Based on Eq. 4 and Eq. 7, we get the abstract form of Galerkin method

$$\text{Find } \mathbf{u}^n \in V_n, \text{ such that: } a(\mathbf{u}^n, \mathbf{v}_i) = L(\mathbf{v}_i). \quad (11)$$

By assuming finite number of test functions  $\mathbf{v}_1, \mathbf{v}_2, \dots, \mathbf{v}_n$ , Galerkin method turns the abstract form into a set of linear equations that can be solved numerically

$$\mathbf{A}\mathbf{u} = \mathbf{b}, \quad (12)$$

where  $A_{ij} = a(\phi_j, \mathbf{v}_i)$ ,  $b_i = L(\mathbf{v}_i)$ . The test functions can be either in  $V_n$  or not, and the type of Galerkin method where  $\mathbf{v}$  is not taken in  $V_n$  is called Petrov-Galerkin method. Galerkin method is more general than Ritz method. Compared to Ritz method, Galerkin method does not require the symmetry of the bilinear form, allowing it to handle problems where the minimization form of PDEs does not exist.

Inspired by these two classical numerical methods, we develop Ritz approach and Galerkin approach of VOL respectively to approximate system functional and residual with deep learning toolkit (see section 5.1 and Fig. 6).

### 3.3 Finite element methods

FEMs is a special case of Ritz method and Galerkin method, where finite subdomains (elements) are designed to be supports of trial functions and test functions. In this Article, VOL utilizes the discretization scheme of FEMs, and handles the global algebraic equation system of FEMs in a matrix-free and iterative manner (see section 5.1).

## 4 Results

Various experimental results are shown and discussed in this section to demonstrate the effectiveness the proposed VOL. Specifically, we investigate VOL on steady heat transfer problem with variable heat source, Darcy flow with variable conductivity, and variable stiffness elasticity (Fig. 1). We first introduce our problem settings briefly. We conduct scaling experiments to investigate the influence of the different data sizes on the performance of VOL. We then conduct the resolution experiments to verify the capability of VOL at different resolutions. We then design two comparative experiments between VOL and iterative methods to verify the generalization benefits of VOL. We also conduct experiments to compare the proposed optimization strategies in VOL with the data-driven strategy.

## 4.1 Problem settings

### 4.1.1 Variable stiffness elasticity

- *General elasticity*

Consider a linear elastic body  $\mathcal{B} \subset \mathbb{R}^3$  (Extended Data Fig. 1a). Let the boundary of the body be  $\mathcal{S} = \mathcal{S}_\sigma \cup \mathcal{S}_u$ . The governing equations and boundary conditions of  $\mathcal{B}$  are

$$\begin{cases} \sigma_{ij,j} + f_i = 0, & \text{in } \Omega \\ \bar{X}_i = \sigma_{ij}n_j, & \text{on } \mathcal{S}_\sigma \\ u_i = \bar{u}_i, & \text{on } \mathcal{S}_u. \end{cases} \quad (13)$$

The weighted integral form of Eq. 13 is

$$\int_{\Omega} (\sigma_{ij,j} + f_i) \delta u_i d\Omega + \int_{\mathcal{S}_\sigma} (\bar{X}_i - \sigma_{ij}n_j) \delta u_i d\mathcal{S} = 0, \quad \forall \delta u_i \in \{v \in C[\Omega]; v = 0 \text{ on } \mathcal{S}_u\}. \quad (14)$$

According to Green's formula,

$$\begin{aligned} \int_{\Omega} \sigma_{ij,j} \delta u_i d\Omega - \int_{\mathcal{S}_\sigma} \sigma_{ij}n_j \delta u_i d\mathcal{S} &= \int_{\Omega} \sigma_{ij,j} \delta u_i d\Omega - \int_{\mathcal{S}} \sigma_{ij}n_j \delta u_i d\mathcal{S} = - \int_{\Omega} \sigma_{ij} \delta u_{i,j} d\Omega \\ &= - \int_{\Omega} \frac{1}{2} \sigma_{ij} (\delta u_{i,j} + \delta u_{j,i}) d\Omega = - \int_{\Omega} \sigma_{ij} \delta \varepsilon_{ij} d\Omega, \end{aligned} \quad (15)$$

Substituting Eq. 15 into Eq. 14, we have

$$\begin{aligned} \int_{\Omega} f_i \delta u_i d\Omega + \int_{\mathcal{S}_\sigma} \bar{X}_i \delta u_i d\mathcal{S} &= \int_{\Omega} \sigma_{ij} \delta \varepsilon_{ij} d\Omega, \\ \forall \delta u_i \in \{v \in C[\Omega]; v = 0, \text{ on } \mathcal{S}_u\}. \end{aligned} \quad (16)$$

Eq. 16 is also known as *the principle of virtual work*, which is a variational form of Eq. 13. The left term of Eq. 16 is the virtual work done by the external forces, and the right term is the strain energy of the elastic body  $\mathcal{B}$  (also the opposite of the virtual work done by the internal forces). Thus, we have

$$\delta W_{\text{int}} + \delta W_{\text{ext}} = -\delta [U + U_e] = 0, \quad (17)$$

where  $\delta W_{\text{int}}$ ,  $\delta W_{\text{ext}}$  are the virtual work done by the internal forces and the virtual work done by the external forces respectively.  $U$  is the strain energy of the elastic body  $\mathcal{B}$ , and  $U_e$  is the potential energy of the external forces. Let the system functional be  $\Pi$ , and we have

$$\begin{aligned} \delta \Pi &= 0, \\ \Pi &= U + U_e, \\ \forall \delta u_i \in \{v \in C[\Omega]; v = 0, \text{ on } \mathcal{S}_u\}. \end{aligned} \quad (18)$$

Note Eq. 18 is equivalent to Eq. 13, and here we only give the derivation of Eq. 18 from Eq. 13.

For convenience, we rewrite the stress tensor and strain tensor in their vector form, i.e.,

$$\boldsymbol{\sigma} = [\sigma_x, \sigma_y, \sigma_z, \tau_{yz}, \sigma_{xz}, \sigma_{xy}]^T, \quad \boldsymbol{\varepsilon} = [\varepsilon_x, \varepsilon_y, \varepsilon_z, \tau_{yz}, \varepsilon_{xz}, \varepsilon_{xy}]^T.$$

Then the strain energy of the elastic body and the potential energy of the external forces is

$$\begin{aligned} U &= \int_{\Omega} \frac{1}{2} \boldsymbol{\varepsilon}^T \mathbf{C} \boldsymbol{\varepsilon} d\Omega, \\ U_e &= - \int_{\Omega} \mathbf{f}^T \mathbf{u} d\Omega - \int_{\mathcal{S}_\sigma} \bar{\mathbf{X}}^T \mathbf{u} d\mathcal{S}. \end{aligned} \quad (19)$$

Thus, functional  $\Pi$  is:

$$\Pi = U + U_e = \int_{\Omega} \frac{1}{2} \boldsymbol{\varepsilon}^T \mathbf{C} \boldsymbol{\varepsilon} d\Omega - \int_{\Omega} \mathbf{f}^T \mathbf{u} d\Omega - \int_{\mathcal{S}_\sigma} \bar{\mathbf{X}}^T \mathbf{u} d\mathcal{S}, \quad (20)$$

where  $\mathbf{C}$  is the matrix of material properties. Note  $\Pi$  is the total potential energy of the system.

In context of operator learning, for example,  $\mathbf{C}$  can be a function of coordinates  $\mathbf{C}(x, y, z)$  in random function spaces, and our goal is to learn an operator learning model, which outputs the displacement field  $\mathbf{u}$  that lets  $\delta\Pi = 0$  hold as close as possible for each input instance with  $\mathbf{C}(x, y, z)$  in the test set. In our experiments, we consider a 2-D variable stiffness case, where  $\mathbf{C} = \mathbf{C}(\theta(x, y))$ .

- *Variable stiffness elasticity*

An elastic variable stiffness square plate with in-plane deformation is considered in our experiments, and it is considered to be made of the fiber reinforced material, as shown in Fig. 1. The thickness of the plate is 0.125mm. Due to spatial variation of fiber orientation, the material property of the plate shows anisotropy. The material property matrix in x-y coordinate system  $\mathbf{C}_{xy}$  can be written as:

$$\mathbf{C}_{xy} = \mathbf{T}^{-1} \mathbf{C}_{12} \mathbf{T}^{-T} \quad (21)$$

where

$$\mathbf{T} = \begin{bmatrix} \cos^2 \theta & \sin^2 \theta & 2 \sin \theta \cos \theta \\ \sin^2 \theta & \cos^2 \theta & -2 \sin \theta \cos \theta \\ -\sin \theta \cos \theta & \sin \theta \cos \theta & \cos^2 \theta - \sin^2 \theta \end{bmatrix} \quad (22)$$

And  $\mathbf{C}_{12}$  is the material property matrix in the principle material coordinates, which is not effected by the fiber angle. Eq. 23 gives the formulation of compliance matrix  $\mathbf{S}_{12}$ , i.e., the inverse of  $\mathbf{C}_{12}$ :

$$\mathbf{S}_{12} = \begin{bmatrix} \frac{1}{E_1} & -\frac{\nu_{12}}{E_1} & 0 \\ -\frac{\nu_{12}}{E_1} & \frac{1}{E_2} & 0 \\ 0 & 0 & \frac{1}{G_{12}} \end{bmatrix} \quad (23)$$

The fiber angle field  $\theta = \theta(x, y)$  of the plate is characterized in two ways as problem settings: (1) Elasticity A: Linear 1-D variation [12, 13]. (2) Elasticity B: B-splines surface [55]. The goal of VOL is to learn the mapping between the fiber angle field space and the vector space of displacement components  $[u_1, u_2]^T$ . Specifically, we study a 100mm  $\times$  100mm fiber-reinforced panel. For details about problem settings of variable stiffness elasticity, including material properties, boundary conditions, elements and parameter range, see Fig 1 and Supplementary material S2.2.

#### 4.1.2 Steady heat transfer with variable heat source and Darcy flow

Steady heat transfer with variable heat source in 1m  $\times$  1m  $\times$  1m cube and Darcy flow with variable conductivity in 1  $\times$  1 square are studied respectively (See Fig. 1). The governing equation of both steady heat transfer and Darcy flow is described as

$$\begin{cases} -\nabla \cdot (\boldsymbol{\kappa} \nabla T) = Q & \text{in } \Omega, \\ T = \bar{T} & \text{on } \mathcal{S}_D, \\ (\boldsymbol{\kappa} \nabla T) \cdot \mathbf{n} = \bar{q} & \text{on } \mathcal{S}_N, \\ (\boldsymbol{\kappa} \nabla T) \cdot \mathbf{n} = \bar{h} (T_\infty - T) & \text{on } \mathcal{S}_R, \end{cases} \quad (24)$$

where  $T$  represents temperature in the variable heat source problem and the hydraulic head in the Darcy flow problem,  $\boldsymbol{\kappa}$  represents conductivity tensor, and  $Q$  is source term. Let  $v$  be test function that satisfies Dirichlet boundary condition, leading to the weak form of Eq. 24

$$\int_{\Omega} [\nabla v \cdot (\boldsymbol{\kappa} \nabla T) - vQ] d\Omega = \int_{\Omega} [\nabla^T v \boldsymbol{\kappa} \nabla T - vQ] d\Omega = 0. \quad (25)$$

When the  $\boldsymbol{\kappa}$  is symmetric, the minimization form of Eq. 24 exists

$$\min_T I = \frac{1}{2} \int_{\Omega} [\nabla^T T \boldsymbol{\kappa} \nabla T - 2QT] d\Omega, \quad (26)$$

where  $T$  satisfies Dirichlet boundary condition.

For variable heat source problem, the goal of VOL is to learn the mapping between heat source field and the temperature field. For Darcy flow problem, the goal of VOL is to learn the mapping between the conductivity field and the hydraulic head. For more details about problem settings of variable heat source problem and Darcy flow problem, see Supplementary material S2.1.

## 4.2 Scaling experiments

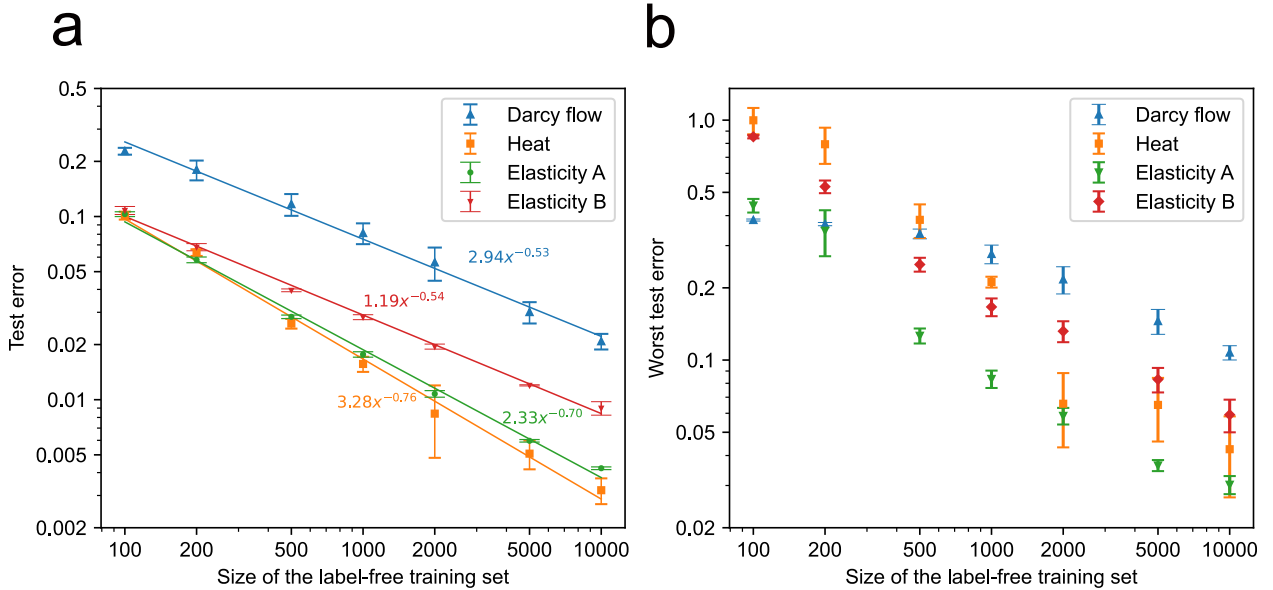


Figure 2: **Results of scaling experiments.** **a**, The test errors for all cases in the scaling experiments show a polynomial convergence rate. The error bars show the one standard deviation from 5 runs with different training/test data initialization.  $x$  is the number of training data. **b**, The worst test errors also decrease in all cases as the size of training data increases.

To verify the effectiveness of VOL with different unlabeled data sizes, we design scaling experiments for all cases in section 4.1 with a specific resolution. For all cases, we chose 7 different sizes for the training set: 100, 200, 500, 1000, 2000, 5000, 10000, and set the size of the test set to 2000. All scaling experiments are conducted with VOL+CG(2) to demonstrate the capability and effectiveness of VOL to learn operators with small update steps. For more details about scaling experiments, see Supplementary material S6.1. With the increase of the number of unlabeled data for training, the performance of VOL should be improved considerably, which has been observed in Fig 2a. With a log scale in data size and test error, an approximately linear convergence versus the size of training set is observed among all cases. From our size scaling results, the test error and the training set size matches a power law, which has also been observed in research about large language models (LLMs) [23, 34] and DeepONet with the data-driven strategy [32],

Darcy flow	Resolution	32	64	128	256	512
	Test error	1.14±0.04	1.25±0.07	1.41±0.08	1.69±0.18	2.21±0.32
Elasticity B	Resolution	33	65	129	257	513 (batch size=8)
	Test error	1.89±0.03	1.92±0.04	1.94±0.04	1.95±0.06	1.89±0.02

Table 2: **Test errors of resolution experiments.**

i.e.,  $y = ax^b$ , where  $y$  refers to the test error and  $x$  refers to the training set size. Related coefficients have also been reported in Fig 2a. In addition to the average metrics of VOL on the test set, we also study the worst-case scenario. Fig 2b shows that the test errors of the worst prediction decrease for all benchmarks as the training set size increases. Extended Data Figure 3, Extended Data Figure 4 and Extended Data Figure 5 visualize the worst predicted samples, which has largest test errors of all problems at ( $N_{\text{training set}} = 10000$ ,  $N_{\text{test set}} = 2000$ ), where we observe VOL still provides approximately correct solution fields.

### 4.3 Resolution experiments

To demonstrate the capability of VOL at different resolutions, we conduct resolution experiments on two problems: the Darcy flow and elasticity B. We keep the size of the training set and the test set at all resolutions be 2000 for these two problems. For experiments at all resolutions in one problem, we use the same model architecture settings. For complete training settings and other details, see Supplementary material S6.2. For darcy problem, we observe the test error slightly rises as the resolution increases. For elasticity B problem, we observe the test error also slightly rises from resolution 33 to resolution  $257 \times 257$ . With resolution  $513 \times 513$ , we observe the test error drops to an average value of 1.89%, we consider which is likely due to the adjustment of batch size at resolution  $513 \times 513$ . Benefited from the resolution-invariant feature of FNOs [28], VOL is able to learn solution operators mostly effectively at different resolutions with the same amount of parameters.

### 4.4 Generalization benefits

From the perspective of the neural solver, the *generalization*, as a unique advantage of the machine learning, especially of the deep learning, can be utilized to provide better initial solutions for the solver solving new problems. In the context of VOL, generalization benefits means that the neural operator module keeps learning and provides more accurate initial solution for the iterative solver. To demonstrate the generalization benefits of VOL, we conduct two experiments, which compare VOL+CG( $i$ ) and CG( $i$ ) on same and different datasets respectively with various numbers of update steps on the elasticity B problem. Specifically, for a comprehensive and fair comparison, we choose restarted conjugate gradient CG( $i$ ) with a set of numbers of update steps,  $i \in \{1, 2, 5, 10, 25, 50, 100\}$ , to compare with VOL that uses the same set of CG update step numbers for these two experiments (VOL+CG( $i$ )) in these two experiments. When  $i = 1$ , conjugate gradient method degenerates itself to one-step steepest decent. We only study SD = CG(1) case for these two experiments, and do not research steepest decent with more update steps, for SD has a well-known slow convergence speed, while more update steps of SD also brings more times of calculating matrix-vector products like CG. We run CG( $i$ ) with its initial guess as the average of labels (CG( $i$ )-A) in the shift set used by VOL and with a random normal distribution initialization (CG( $i$ )-R) independently. For every epoch, CG( $i$ ) solves each sample in the training set with  $i$  update steps and restarts itself for the next epoch. We conduct these two experiments at resolution  $33 \times 33$ ,  $129 \times 129$  and  $257 \times 257$ . See Supplementary material S6.3 for more details of the experimental design.

For the first experiment, we compare VOL and restarted conjugate gradient method on a same dataset containing 2000 samples, as shown in Fig. 3a to Fig. 3c. We set no test set for VOL in this experiment. At

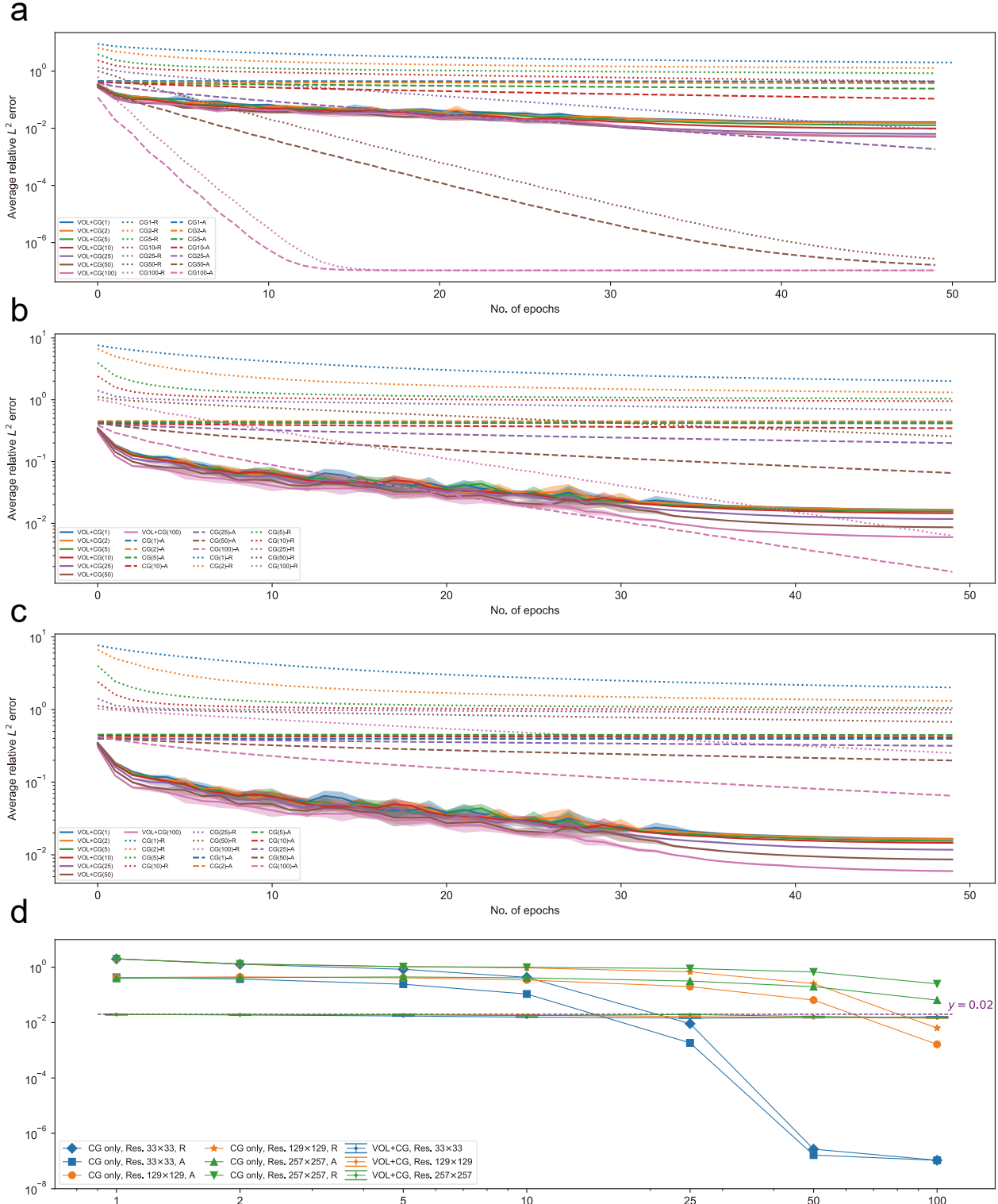


Figure 3: **Comparison on VOL and classical iterative methods.** **a, b, c,** Average relative  $L^2$  errors on the training set are recorded for every epoch in the first experiment. **a, b, c** are the training errors at resolution  $33 \times 33$ ,  $129 \times 129$ ,  $257 \times 257$  respectively. The shaded regions denote one standard deviation. **d,** We plot  $y = 0.02$  as a reference line VOL+CG( $i$ ). As the number of update steps increases, the test error of VOL+CG( $i$ ) decreases slowly, from coinciding with  $y = 0.02$  to gradually falling below it.

resolution  $33 \times 33$ , when the number of update step is set to 1, 2, 5, 10, the train error of VOL is approximately one order of magnitude smaller than restarted CG at then end of iterations. As the number of update steps increases, restarted CG starts to converge faster. At resolution  $33 \times 33$ , restarted CG has a faster convergence speed than VOL at 25, 50, 100 update steps, and has also a far smaller average train errors than VOL at 50 and 100 update steps at the end of training. At higher resolutions, however, classical iterative methods converge much slower. For resolution  $257 \times 257$ , compared with  $CG(i)$ -R, the training errors of  $VOL+CG(i)$  are approximately one order to even two orders of magnitude smaller for all considered update steps at the end of iterations. Compared with  $CG(i)$ -A,  $VOL+CG(i)$  also has around one order of magnitude smaller training errors at the end of iterations. From Fig. 3a to Fig. 3c, we observe the error lines of  $CG(i)$ -R and  $CG(i)$ -A with the same update step are nearly parallel before their convergence, which indicates that, in our case, the difference of initialization has no significant effect on the convergence speed of the restart conjugate gradient method. We also note that generalization benefits, which can improve the magnitude of test errors, do not significantly improve the convergence speed of  $VOL+CG(i)$ . In fact, the condition number of coefficient matrix  $\mathbf{K}$  is the key factor affecting convergence speed [40]. We discuss possible solutions to accelerate the convergence as our future work (see section 6).

To verify the competitiveness of generalization for unseen data of VOL against the classical restarted iterative method, we conduct the second experiment, where the neural operators are first trained with  $VOL+CG(i)$  on a 2000-sample training set, and then tested on a separate 2000-sample test set at the same resolution. Results (Fig. 3d) show that VOL can generalize to unseen data at various resolutions with different update step numbers, and the superiority of VOL becomes more and more obvious as the resolution grows. However, we also observe that VOL improves but has no significant improvement on the test error as the number of update steps grows, which needs further investigation.

#### 4.5 Comparison on different optimization strategies

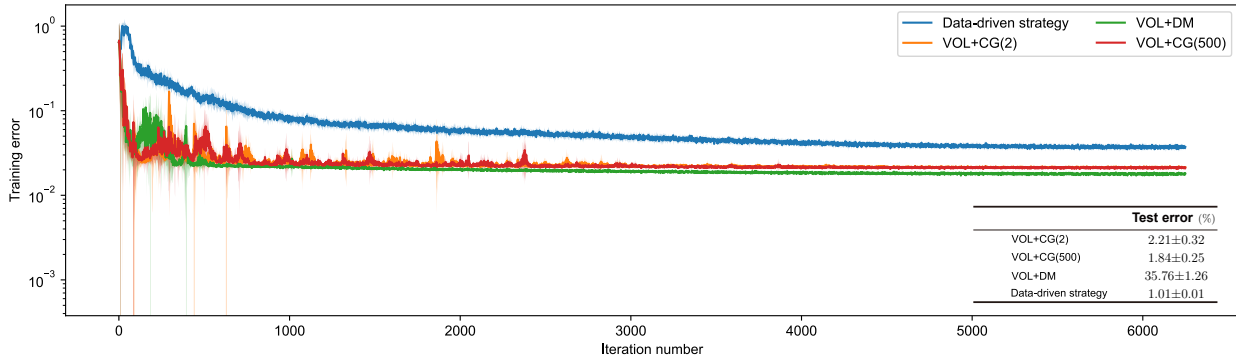


Figure 4: **Comparison on different optimization strategies.** For all strategies, the training error is set as average residual norm per batch, and is recorded for every iteration step. In this figure we also report the test errors (average relative  $L^2$  error) at the lower right corner.

In this section, we compare different optimization strategies for training neural operators with experimental results and discussion. We consider three strategies, iterative update ( $VOL+CG$ ), direct minimization ( $VOL+DM$ ), and purely data-driven strategy. For  $VOL+CG$ , we also chose 2 and 500 conjugate update steps respectively for VOL to further investigate the effect of update step number on performance of VOL. For all strategies, the experiment is conducted on Darcy flow problem at  $512 \times 512$  resolution, with 2000 training data and 2000 test data. To ensure a fair comparison, we keep all training settings (number of epochs, learning rate, scheduler, batch size, etc., for details see Supplementary material S6.4) same for each

strategy. We observe no significant difference between VOL+CG(2) and VOL+CG(500) in training, but for test error VOL+CG(500) is a bit better than VOL+CG(2) on average. We then observe that while the converged residual norm of each strategy satisfies relationship "data-driven strategy > VOL+CG > VOL+DM", the relationship of test errors is the exact opposite of that, which is "data-driven strategy < VOL+CG < VOL+DM". For the data-driven strategy, the residual norm first rises to  $\sim 10^0$ , and then decreases with a steep slope. As the training proceeds, the slope of the data-driven strategy steadily gets smaller until the end of training. For VOL+CG and VOL+DM, however, no rise of the residual norm was observed at start. In contrast, a sharp drop of the residual norm is observed from the very beginning of the training ( $\sim 10$  steps) for VOL+CG and VOL+DM. After the sharp drop, the residual norm of both VOL+CG and VOL+DM falls a bit in significant fluctuations. The distinguishable fluctuations of VOL+DM almost stop after  $\sim 1000$  iterations, while that of the VOL+CG stop after  $\sim 3000$  iterations. We also notice that though VOL can achieve a smaller residual norm than the data-driven strategy, the residual norm nearly stagnated after initial progress. In section 5.2, we propose that VOL+CG can be interpreted as training neural operator module with provisional labels. Provisional labels, as intermediate solutions provided by the iterative solver, contain noise and are not accurate as ground truth labels, which might explain the gap of performance on test set between VOL and data-driven strategy. From experimental results, we also observe direct minimization has the worst test error in all strategies. Different from the strong form case [44, 37], it might not be a good choice to penalize the residual by putting it in the loss function in our finite element settings. In fact, we can prove that VOL+DM strategy feeds the direct iterative update on the normal equation of the original linear system to the neural operator module (see Supplementary material S8 for proof), which might explain the gap of performance on test set between VOL+DM and other strategies. It is also noted that, even though comparative experiments show all strategies of VOL have larger average test errors than the data-driven strategy, the test errors of VOL+CG are just passable.

## 5 Methods

In this section, the variational operator learning (VOL) algorithm is developed. VOL does not focus on creating novel neural operator architectures, instead, it focuses on training the existing state-of-the-art neural operators with the smallest possible amount of labeled data, even no label. VOL is applicable to *any field-wise neural architecture* in principle, but for the purpose of a clear demonstration of the basic effectiveness of VOL, in all experiments we just employ the Fourier neural operator (FNO) [28] in the neural operator module of VOL with moderate modification. Related network flowchart is shown in Fig. 5a.



---

**Algorithm 1 Variational operator learning algorithm**

---

**Input:** neural operator module  $\mathcal{N}_{operator}(\vartheta)$ , number of epochs  $N$ , optimization strategy  $Opt$ , learning rule  $\eta$ , and training set  $\mathcal{D}=\{\mathbf{U}_i\}_{i=1}^{N_{train}}$ , max iteration number of one epoch  $maxiter$ , mask operation  $Mask$ , Shift set  $Shift$ , network optimizer  $Opt_{net}$  and learning rate scheduler  $Scheduler$

```
1: for  $1 \leq i \leq N$  do
2:   for  $1 \leq j \leq maxiter$  do
3:     Sample a minibatch of  $bs$  examples  $\mathbf{U}_j^{bs}$  from  $\mathcal{D}$ 
4:      $\mathbf{a}_j^{bs} = \mathcal{N}_{operator}(\vartheta) \left( \mathbf{U}_j^{bs}, Mask, Shift \right)$ 
5:     Get  $\mathbf{R}_j^{bs}$  with Ritz approach or Galerkin approach
6:      $\mathbf{R}_j^{bs} = Mask \left( \mathbf{R}_j^{bs} \right)$ 
7:      $\Delta \mathbf{a}_j^{bs} = Opt \left( \mathbf{R}_j^{bs}, \mathbf{a}_j^{bs}, \mathbf{U}_j^{bs}, Mask \right)$ 
8:     Get the current learning rate  $\hat{\eta}$  according to  $\eta$  and  $Scheduler$ 
9:     Update  $\vartheta$  with  $\Delta \mathbf{a}_j^{bs}$ ,  $Opt_{net}$  and  $\hat{\eta}$ 
10:  end for
11: end for
```

**Return:** learned neural operator module  $\mathcal{N}_{operator}(\vartheta)$

---

The proposed VOL can be seamlessly integrated into deep learning training pipeline. The Algorithm 1 demonstrates a complete training process including the outer epoch loop and the inner dataset loop. Here we just start discussion at the inner loop.

Line 4 of the Algorithm 1 shows a standard forward propagation from unlabeled input parameters to the node solution. Each channel of the node solution tensor contains one component of the node solution. Parameters of PDEs are first discretized at Gauss points and nodes, and then are aggregated into the parameter tensor  $Para|_G$  and  $Para|_N$  respectively (Fig. 5b). For  $Para|_G$ , parameters at Gauss points that at the same position of all elements are encoded into one channel of the parameter tensor. Thus, the number of the channel of the parameter tensor equals to number of Gauss points in one element, and the resolution of  $Para|_G$  is equal to the mesh size. For  $Para|_N$ , one channel of parameter tensor corresponds to one component of the parameter. For a concerned parameter of PDEs, the neural operator module (Fig. 5a) receives  $Para|_G$  or  $Para|_N$  as input. Light feature engineering is first adopted for the input parameter tensor. The alignment operation (Fig. 5c) is needed only for  $Para|_G$  input, which is implemented with a trainable transposed convolution, mapping the tensor from the mesh size to the node size. Then, the lifting layer lifts the tensor to a higher channel space,  $N$  Fourier layers are adopted, and the projection layer projects tensor to the solution space, which is the main operations of FNO [28]. Two additional operations are performed on the node solution predicted by the neural operator module:

(1) Mask operation. The mask operation is designed to apply the essential boundary condition, such as displacement boundary condition in elasticity and temperature boundary condition in heat transfer to the system, which is equivalent to the constraint imposition process in the FEMs. First, a mask tensor that contains 0 and 1 is constructed, which has the same shape as the node solution. Every element in the mask tensor corresponds to a certain degree of freedom of a certain node in the computational mesh. If an element of the mask tensor is "0", it means that the corresponding degree of freedom of the corresponding node is constrained, while "1" means not constrained. Then, the element-wise product between the solution tensor and the mask tensor is calculated, as shown in Fig. 5d. The technique of the mask operation can be categorized into the so-called *hard* manners [47, 9, 39] to enforce the boundary condition of PDEs, which is different to the *soft* manner, where the BCs are treated as penalty terms in the loss function. The mask operation can also be extended to the inhomogeneous case. As shown in Fig. 5d, we simply add

a shift tensor with the same shape after the element-wise product operation, the elements of which are 0 where the corresponding elements of the mask tensor are 1 (unconstrained), and the other elements are the inhomogeneous terms of constraints.

(2) Distribution-shift. Distribution-shift operation that exists in the prior work [28, 53] is remained in this work, but we only use a very small number labeled data (5 labels) rather than label the whole training set. It first computes the mean *mean* and the standard deviation *std* of all labels of the training set, and then use the following equation to shift the output of the neural operators to the distribution of the labels:

$$output = output \otimes std + mean \quad (27)$$

Such a shift operation can stabilize the training process. Note the training set is totally label-free. To generate labels for the shift operation, an extra small batch of parameters of PDEs are randomly sampled and labeled, and these labeled data are only used in the distribution-shift operation, which we call a *shift set*.

## 5.1 Matrix-free approximation of the system functional and the system residual

In line 5 of Algorithm 1, Ritz approach and Galerkin approach of VOL are developed respectively to approximate the system functional and the system residual. In this section, we introduce these two approaches with theory consideration and implementation details.

### 5.1.1 Ritz approach

Ritz approach of VOL is composed of two parts, system functional approximation (forward propagation) and residual calculation (backpropagation). Ritz approach is matrix-free and can approximate system functional and system residual numerically. In this section, an approximation of the system functional used by Ritz approach is first introduced with the context of elasticity, the formulation of which is a bit different from that in FEMs, making VOL possible to approximate system functional without calculating stiffness matrices. Then, we introduce how to calculate system functional numerically with deep learning toolkit and the residual calculation. It is worth noting that it is possible for VOL to use various discretization scheme, notwithstanding VOL uses the same discretization scheme (piecewise polynomial interpolation) as FEMs in this Article:

$$\begin{aligned} \mathbf{u}(x, y, z) &= \mathbf{N}(r, s, t) \mathbf{a}^e, \\ \mathbf{x} &= \mathbf{N}(r, s, t) \mathbf{x}^e. \end{aligned} \quad (28)$$

Note  $\mathbf{u}(x, y, z)$  and  $\mathbf{a}^e$  are node-related quantities, they can represent the displacement in the context of solid mechanics, and the temperature in heat transfer, etc.

We take an elastic body discretized by isoparametric elements as an example. In this case, the node solution is the node displacement tensor of the elastic body. The classical expression of functional approximation in FEMs is:

$$\begin{aligned} \tilde{\Pi} = \sum_e \Pi^e &= \frac{1}{2} \sum_e \left( \mathbf{a}^{eT} \int_{\Omega_e} \mathbf{B}^T \mathbf{D} \mathbf{B} d\Omega \mathbf{a}^e \right) \\ &\quad - \sum_e \left( \mathbf{a}^{eT} \int_{\Omega_e} \mathbf{N}^T \mathbf{f} d\Omega \right) - \sum_e \left( \mathbf{a}^{eT} \int_{S_\sigma^e} \mathbf{N}^T \bar{\mathbf{X}} dS \right). \end{aligned} \quad (29)$$

The  $\int_{\Omega_e} \mathbf{B}^T \mathbf{D} \mathbf{B} d\Omega$ ,  $\int_{\Omega_e} \mathbf{N}^T \mathbf{f} d\Omega$  and  $\int_{S_\sigma^e} \mathbf{N}^T \bar{\mathbf{X}} dS$  in Eq. 29 are element stiffness matrix, element volume load vector and element face load vector respectively. Denote them as

$$\mathbf{K}^e = \int_{\Omega_e} \mathbf{B}^T \mathbf{D} \mathbf{B} d\Omega, \quad \mathbf{P}^e = \int_{\Omega_e} \mathbf{N}^T \mathbf{f} d\Omega + \int_{S_\sigma^e} \mathbf{N}^T \bar{\mathbf{X}} dS. \quad (30)$$

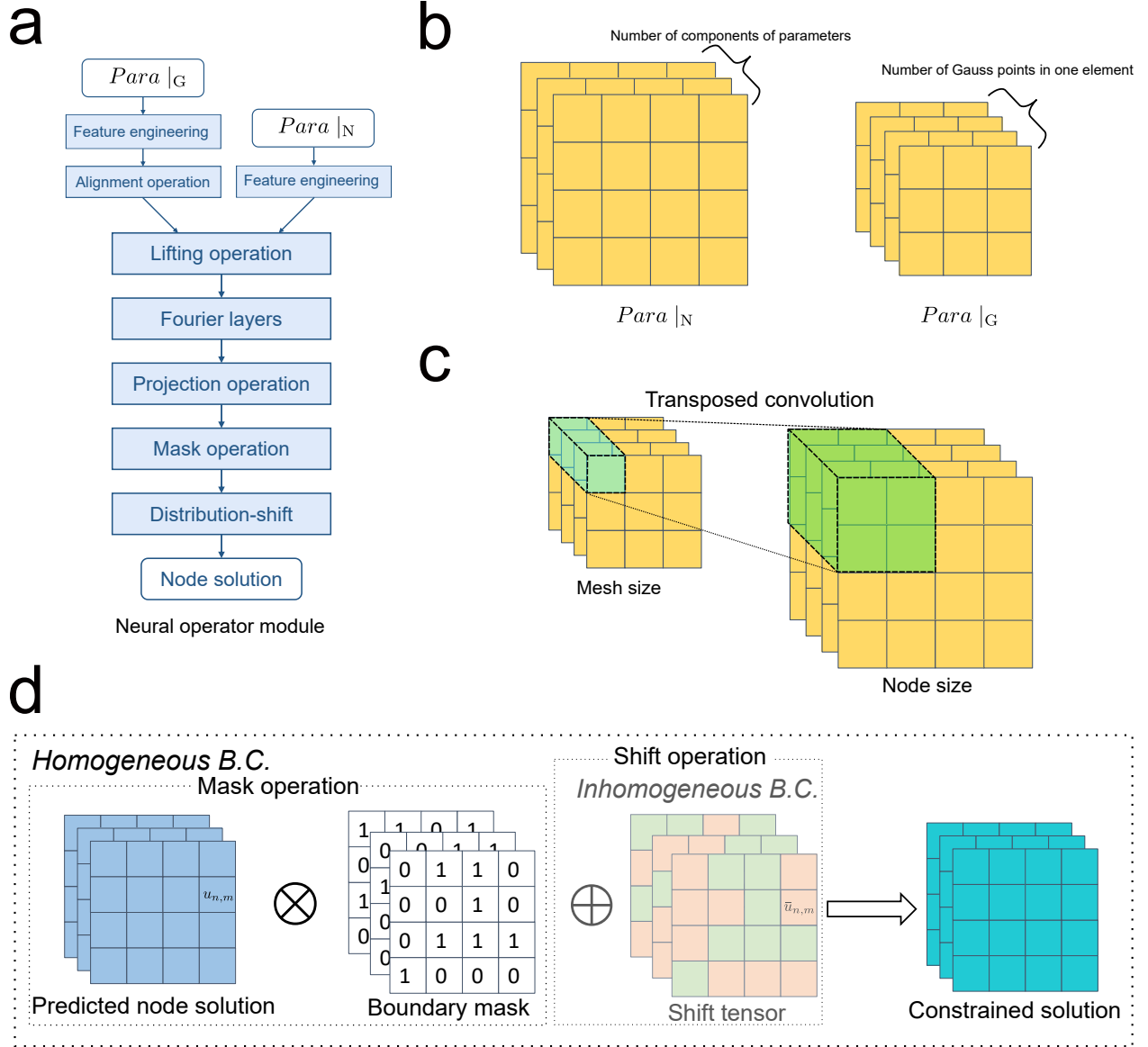


Figure 5: **Neural operator module and the related operations.** **a**, The neural operator module in the framework of VOL. **b**, Parameter tensor ( $Para |_G$ , left) aggregated by parameters discretized at Gauss points and parameter tensor ( $Para |_N$ , right) aggregated by parameters discretized at nodes. **c**, The alignment operation in the neural operator module. **d**, Mask operation and shift operation. The homogeneous essential boundary conditions can be applied to the node solution by the mask operation. For shift operation, the inhomogeneous boundary condition can be then applied with a shift tensor, where the red elements denote the inhomogeneous terms, and the green elements denote zeros. For example, as shown in the figure,  $u_{n,m}$  is the predicted solution to the  $n$ th degree of freedom of the  $m$ th node, the corresponding element of which in the mask tensor is 0. And the corresponding element in the shift tensor is  $\bar{u}_{n,m}$ , which denotes the inhomogeneous term of the constraint of  $n$ th degree of freedom of  $m$ th node.

We have

$$\tilde{\Pi} = \frac{1}{2} \mathbf{a}^T \sum_e (\mathbf{G}^{eT} \mathbf{K}^e \mathbf{G}^e) \mathbf{a} - \mathbf{a}^T \sum_e (\mathbf{G}^{eT} \mathbf{P}^e), \quad (31)$$

and

$$\mathbf{K} = \sum_e \mathbf{G}^{eT} \mathbf{K}^e \mathbf{G}^e, \quad \mathbf{P} = \sum_e \mathbf{G}^{eT} \mathbf{P}^e. \quad (32)$$

In FEMs, element stiffness matrices in Eq. 30 are first obtained by numerical integration and then are assembled together with Eq. 32 to form the global stiffness matrix. On the other hand, the whole process of Ritz approach is *matrix-free*, i.e., it does not calculate any stiffness matrices or restore them, which is elaborated in the following paragraphs. The formulation of element stiffness matrix given by Gaussian quadrature method is:

$$\mathbf{K}^e = \int_{\Omega_e} \mathbf{B}^T \mathbf{D} \mathbf{B} d\Omega \approx \sum_{l=1}^{n_g} H_l \mathbf{B}_l^T \mathbf{D}_l \mathbf{B}_l |\mathbf{J}_l^e|. \quad (33)$$

Similarly,

$$\mathbf{P}^e \approx \sum_{l=1}^{n_g} H_l \mathbf{N}_l^T \mathbf{f}_l |\mathbf{J}_l^e| + \sum_{m=1}^{n_{S_\sigma^e}} \sum_{l=1}^{n_m} I_{ml} \mathbf{N}_{ml}^T \bar{\mathbf{X}}_{ml} \left| \mathbf{J}_{ml}^{S_\sigma^e} \right|. \quad (34)$$

Substitute Eq. 33, Eq. 34 into Eq. 29, and note

$$\boldsymbol{\varepsilon} = \mathbf{B} \mathbf{a}^e. \quad (35)$$

Then we have another kind of formulation to express the functional, which is slightly different from Eq. 29 and Eq. 31:

$$\begin{aligned} \tilde{\Pi} &= \sum_e \Pi^e \approx \frac{1}{2} \sum_e \sum_{l=1}^{n_g} H_l \mathbf{a}^{eT} \mathbf{B}_l^T \mathbf{D}_l \mathbf{B}_l \mathbf{a}^e |\mathbf{J}_l^e| \\ &\quad - \sum_e \sum_{l=1}^{n_g} H_l \mathbf{a}^{eT} \mathbf{N}_l^T \mathbf{f}_l |\mathbf{J}_l^e| - \sum_e \sum_{m=1}^{n_{S_\sigma^e}} \sum_{l=1}^{n_m} I_{ml} \mathbf{a}^{eT} \mathbf{N}_{ml}^T \bar{\mathbf{X}}_{ml} \left| \mathbf{J}_{ml}^{S_\sigma^e} \right| \end{aligned} \quad (36)$$

or

$$\begin{aligned} \tilde{\Pi} &= \sum_e \Pi^e \approx \frac{1}{2} \sum_e \sum_{l=1}^{n_g} H_l \boldsymbol{\varepsilon}_l^T \mathbf{D}_l \boldsymbol{\varepsilon}_l |\mathbf{J}_l^e| \\ &\quad - \sum_e \sum_{l=1}^{n_g} H_l \mathbf{a}^{eT} \mathbf{N}_l^T \mathbf{f}_l |\mathbf{J}_l^e| - \sum_e \sum_{m=1}^{n_{S_\sigma^e}} \sum_{l=1}^{n_m} I_{ml} \mathbf{a}^{eT} \mathbf{N}_{ml}^T \bar{\mathbf{X}}_{ml} \left| \mathbf{J}_{ml}^{S_\sigma^e} \right| \end{aligned}$$

Ritz approach uses formulations like Eq. 36 to approximate functional, while FEMs use Eq. 29 or Eq. 31. It is clear that neither the element stiffness matrix nor the global stiffness matrix appears in Eq. 36. Thus, to calculate Eq. 36, the calculation and the assembly process of the element stiffness matrices can be simply skipped.

According to Eq. 18 and Eq. 28, the node solution field should satisfy

$$\delta \tilde{\Pi} = \frac{\partial \tilde{\Pi}}{\partial a_1} \delta a_1 + \frac{\partial \tilde{\Pi}}{\partial a_2} \delta a_2 + \cdots + \frac{\partial \tilde{\Pi}}{\partial a_{n_f}} \delta a_{n_f} = 0 \quad (37)$$

Eq. 37 is also called the *stationary condition* of  $\tilde{\Pi}$ . Since  $\delta a_1, \delta a_2, \cdots, \delta a_{n_f}$  are the virtual displacement of nodes, we have

$$\frac{\partial \tilde{\Pi}}{\partial \mathbf{a}} = \mathbf{0} \quad (38)$$

Substituting Eq. 31 and Eq. 32 into Eq. 38, we have

$$\mathbf{K}\mathbf{a} = \mathbf{P} \quad (39)$$

FEMs approximate the functional (Eq. 31), perform variational operation (Eq. 38) *offline*, form and solve Eq. 39 *online*. On the other hand, Ritz approach approximates the functional (Eq. 36) and performs the variational operation *online* after every forward propagation. Ritz approach of VOL performs the variational operation to get the residual  $\mathbf{R}$  of the predicted node solution field:

$$\mathbf{R} = \frac{\partial \tilde{\Pi}}{\partial \mathbf{a}} = \mathbf{K}\mathbf{a} - \mathbf{P} \quad (40)$$

The deep Ritz method [7] and the literature [41] also construct the system functional, but they just simply set functional minimization as the goal of optimization (minimization form), that is, they treat the system functional as the loss function in deep learning pipeline. Compared to the idea of deep Ritz method, our approach goes a step further. Rather than minimize the functional directly, we choose to set minimizing the norm of residual that derived from the variational operation as the optimization objective. Apart from a basic strategy of setting the norm of the residual itself as the loss function, we also turn to solve the corresponding linear system with iterative methods, by utilizing the connection between the computational mesh (see Extended Data Figure 2), the residual and the linear system to minimize the norm of the residual. Such a scheme allows us to train on a mesh. (see section 5.2 for details of optimization strategy of VOL)

Four steps are needed to conduct numerical integration and get the system functional approximation of Eq. 36 in the forward propagation of Ritz approach:

(1) Calculate the weighted sum of  $\mathbf{a}^e$  and other types of node-related physical quantities (such as discrete parameter field at nodes) weighted by the interpolation function and its spatial derivatives at Gauss points. Here we introduce the weighted sum of node solution. The same operations will be performed on other types of node-related physical quantities if needed in VOL. Observe Eq. 28, the left term of which can be seen as the weighted sum of  $\mathbf{a}^e$ :

$$u_i = \sum_{j=1}^M N_j a_{j,i}^e, \quad (41)$$

and take the derivative of both sides

$$\frac{\partial u_i}{\partial \mathbf{x}} = \sum_{j=1}^M \mathbf{J}^{e-1} \frac{\partial N_j}{\partial \mathbf{r}} a_{j,i}^e. \quad (42)$$

Eq. 41 and Eq. 42 are essentially equivalent to convolution operations on discrete node solution field, if the weight of the convolution filters is set as values of terms  $N_j$  and  $\mathbf{J}^{e-1} \frac{\partial N_j}{\partial \mathbf{r}}$  at Gauss points. On this basis, we develop the method of calculating Eq. 41 and Eq. 42 based on the standard non-trainable convolution operation, which is implemented easily with tensor-based deep learning engines:

- ① Compute the value of  $N_j$  and  $\mathbf{J}^{e-1} \frac{\partial N_j}{\partial \mathbf{r}}$  at Gauss points, organize and restore them as convolution filters, which we name a trial kernel  $\mathcal{K}_{\text{trial}}$ . The trial kernel reflects the ansatz of the trial function.
- ② Convolve  $\mathbf{a}$  with the  $\mathcal{K}_{\text{trial}}$ , unit stride and no padding to get the feature map at Gauss points:  $[u_i |_{\mathbf{G}}, \frac{\partial u_i}{\partial \mathbf{x}} |_{\mathbf{G}}] = \mathcal{K}_{\text{trial}} \circledast \mathbf{a}$ .

An illustrative example of weighted sum convolution and calculating  $\mathcal{K}_{\text{trial}}$  is given in Fig. 6a and Fig. 6d respectively.

(2) Calculate the integrand. In step (1), we get two types of weighted sum at Gauss points of all elements, i.e.,  $u_i$  and  $\frac{\partial u_i}{\partial x_j}$ , that gathered as tensors. In this step, as shown in Fig. 6b, these weighted sum tensors are first reorganized into feature maps  $\mathcal{F}_{\text{physics}}$  of physical properties in problems of concern (see section 4.1.1) to facilitate the calculation of integrand with Eq. 36 and the following Galerkin approach. Then, the integrand is then formed by calculating Eq. 36 with  $\mathcal{F}_{\text{physics}}$ . The process utilizes the idea of *domain knowledge embedding* in the section 2. Note that this step varies in implementation details for governing equations in different domains.

(3) Multiply Jacobian (Fig. 6c). The Jacobian tensor that contains the values of the Jacobian at Gauss points of all elements is pre-computed, according to the configuration of all elements in the physical space. Then, the element-wise product of the integrand tensor and the Jacobian tensor are computed to obtain the integrand tensor that considers Jacobian effect.

(4) Calculate the functional approximation of the system with numerical integration (Fig. 6c). First, perform Gaussian quadrature for all elements, i.e., calculate weighted sum of the integrand by weight of Gauss points in every element. The element of result tensor is the functional approximation of the element  $\Pi^e$ . Then, sum up  $\Pi^e$  of all elements to get the functional approximation  $\tilde{\Pi}$ .

Since the forward propagation from node solution to the functional has been constructed, the gradient of the functional to the node solution can be easily derived with automatic differentiation. A backward propagation from the functional to the node solution is conducted, to obtain the gradient of the functional with respect to the node solution. The gradient of the functional to the node solution is just the residual of the linear system, so it is denoted as the residual tensor  $\mathbf{R}$ .

As discussed above, a forward-backward propagation loop between the node solution and the functional approximation has been constructed. The developed loop allows us to derive the residual of the linear system without acquiring element stiffness matrices and assembling the global stiffness matrix. The residual tensor  $\mathbf{R} = \frac{\partial \tilde{\Pi}}{\partial \mathbf{a}}$  is derived by just running the loop once, which has the same shape as the node solution.

### 5.1.2 Galerkin approach

In this section, Galerkin approach is introduced. Galerkin approach is another matrix-free method in VOL of calculating matrix-vector product. Compared to Ritz approach, Galerkin approach is much simpler and applicable even when the minimization form of PDEs does not exist. In contrast to Ritz approach, which follows  $\mathbf{a} \rightarrow \tilde{\Pi} \rightarrow \mathbf{R}$  procedure, Galerkin approach can derive  $\mathbf{R}$  without calculating  $\tilde{\Pi}$  and backpropagation.

Like Ritz approach, Galerkin approach also needs  $\mathcal{F}_{\text{physics}}$ . So it also shares exactly the same convolution operation and kernel  $\mathcal{K}_{\text{trial}}$  as Ritz approach to calculate  $\mathbf{a}|_G$  and  $\frac{\partial \mathbf{a}}{\partial \mathbf{x}}|_G$ . Following classical Galerkin method, Galerkin approach first constructs the test function  $\mathbf{v}$  in the deep learning engine. Here we simply consider  $\mathbf{v}$  as the basis of  $V_n$ . Observing  $\mathbf{v}$  of one node in Fig. 6d, which has compact support and is non-zero over the adjacent elements of the node, we find it possible to arrange value  $\mathbf{v}$  and  $\frac{\partial \mathbf{v}}{\partial \mathbf{x}}$  at Gauss points into groups of filters according to the following rules:

- (1) For each component of  $\mathbf{v}$  and  $\frac{\partial \mathbf{v}}{\partial \mathbf{x}}$ , the value at the same Gauss point of all adjacent elements of the node is put into a separate filter.
- (2) Value from different elements is arranged in the same order for all filters.

We name the filters as the test kernel  $\mathcal{K}_{\text{test}}$ , a 2-dim example of which is given in 6d. Sometimes we may need to construct more sophisticated filters than  $\mathbf{v}$  and  $\frac{\partial \mathbf{v}}{\partial \mathbf{x}}$ . For example, in elasticity we need to construct virtual strain as a test kernel  $\mathcal{K}_{\text{test}} = \delta \varepsilon = \frac{1}{2}(v_{i,j} + v_{j,i})$ . In this regard, we just calculate the components of the desired virtual quantity.

After constructing  $\mathcal{K}_{\text{test}}$ , we can express the weak form of Eq. 4 with a single standard convolution operation on  $\mathcal{F}_{\text{physics}}$  with the kernel  $\mathcal{K}_{\text{test}}$  (Fig. 6e). We also need to use the Jacobian tensor to scale  $\mathcal{F}_{\text{physics}}$

before the convolution. To ensure that our operation is valid for nodes on the boundary, we need to add a zero padding to  $\mathcal{F}_{\text{physics}}$ , which represent a layer of elements wrapped around the solution domain with their  $\mathcal{F}_{\text{physics}}$  set to 0. The convolution stride is set to 1.

In VOL, we use Ritz approach to calculate quadratic forms in SD and CG iterations. System residual and other matrix-vector product (like  $\mathbf{K}\mathbf{p}$  in Algorithm 2 and 3) are mainly calculated with Galerkin approach. We do not use Ritz approach to calculate system residual because doing so would bring additional backpropagation operations and cannot be extended to more general cases where the minimization form of PDEs do not exist.

## 5.2 Optimization strategy

The optimization objective of VOL is to find parameters of the neural operator that minimize the average of residual norm of the whole training set:

$$\begin{aligned} \min_{\mathbf{a}_i} \frac{1}{D} \sum \|\mathbf{R}_i\|_{i=1}^D \\ \text{s.t. } \mathbf{R}_i = \mathbf{K}\mathbf{a}_i - \mathbf{P} \end{aligned} \quad (43)$$

For implementation, the residual  $\mathbf{R}$  is treated as a tensor. Thus, we just calculate the norm of the flattened  $\mathbf{R}$  as the residual norm. The element of the residual tensor is the just the residual of corresponding equation of the linear system Eq. 39, the same one that solved by FEMs, as shown in Extended Data Fig. 2. Thus, the goal of VOL (Eq. 43) has turned to solve all linear systems derived from the parameters of PDEs in the training set. Note that the residual tensor  $\mathbf{R}$  now contains all residuals of the linear system. We need to zero out those elements in  $\mathbf{R}$  that correspond to the constrained part of  $\mathbf{a}$ , so that the coefficient matrix of the linear system is non-singular. Thus, an additional mask operation (Fig. 5) needs to be imposed on the residual tensor  $\mathbf{R}$  in line 6.

In the framework of VOL, we mainly consider two optimization strategies, direct minimization (VOL+DM) and iterative update to optimize Eq. 43.

- *Direct minimization.* VOL+DM sets the residual norm as the loss function directly, which is similar to many existing domain knowledge embedding methods [37, 9, 38]. But according to our experimental results, see section 4.5, VOL+DM performs not as great as the iterative update.
- *Iterative update.* In this Article, we consider two common cases of the iterative update, i.e., the steepest decent update (SD) and the conjugate gradient update (CG). They are wrapped as *Opt* used in line 7 of Algorithm 1. Instead of running the iterative method until it converges, we only use a fixed number of update steps of the iterative method in one forward propagation, which is more computationally efficient and proves to be effective in our experiments (See section 4.2, where VOL+CG(2) shows a power law). SD and CG with  $n$  steps update are shown in Algorithm 2 and Algorithm 3 respectively. They take all of the residual tensors of  $j$ th batch  $\mathbf{R}_j^{bs}$ , the prediction of current batch  $\mathbf{a}_j^{bs}$  and input parameter  $\mathbf{U}_j^{bs}$  as input, and return the update of current prediction  $\Delta\mathbf{a}_j^{bs}$ . To calculate  $\mathbf{R}^T\mathbf{K}\mathbf{R}$  in Algorithm 2 and  $\mathbf{p}^T\mathbf{K}\mathbf{p}$  in Algorithm 3, it is also unnecessary to obtain  $\mathbf{K}$ . All we need to do is to use Ritz approach to  $\mathbf{R}$ , even with a more simplified calculation than Eq. 36:

$$\begin{aligned} \mathbf{R}^T\mathbf{K}\mathbf{R} &= \sum_e \sum_{l=1}^{n_g} H_l \mathbf{R}^{eT} \mathbf{B}_l^T \mathbf{D}_l \mathbf{B}_l \mathbf{R}^e |\mathbf{J}_l^e| \\ \mathbf{p}^T\mathbf{K}\mathbf{p} &= \sum_e \sum_{l=1}^{n_g} H_l \mathbf{p}^{eT} \mathbf{B}_l^T \mathbf{D}_l \mathbf{B}_l \mathbf{p}^e |\mathbf{J}_l^e| \end{aligned} \quad (44)$$

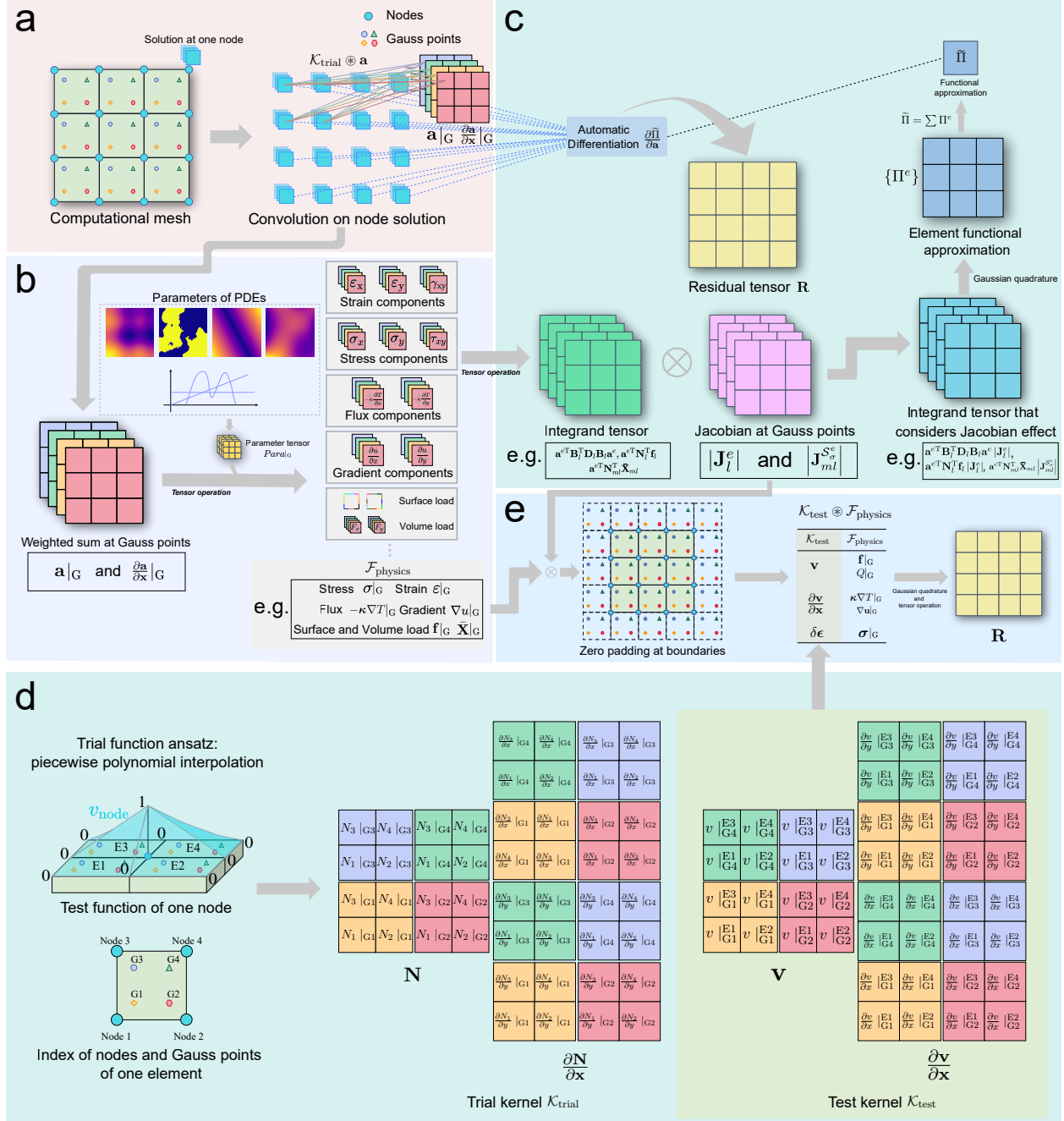


Figure 6: **Ritz approach and Galerkin approach of VOL.** In this figure, we introduce Ritz and Galerkin approach on a domain discretized by 9 quadrilateral elements with 4 nodes and 4 Gauss points as an example. **a**, Evaluation of the weighted sum of node solution at Gauss points with the convolution. Note node solution may have more than one component, and convolution operation on one component is plotted here for simplicity. In **a**, the width×height of one filter is 2×2, and 4 filters are needed. The shape of a weighted sum tensor is 4×3×3. **b**, Calculation of feature maps of physical properties  $\mathcal{F}_{\text{physics}}$ . Parameter tensor, and From **a** and  $\frac{\partial \mathbf{a}}{\partial \mathbf{x}}$  and a feature map of a component of physical properties **c**, System functional approximation and automatic differentiation in Ritz approach. Integrand tensor, Jacobian both have a shape of 4×3×3.  $\{\Pi^e\}$  has a shape of 1×3×3. **d**, The construction of  $\mathcal{K}_{\text{trial}}$  and  $\mathcal{K}_{\text{test}}$ . **e**, The convolution between  $\mathcal{K}_{\text{test}}$  and  $\mathcal{F}_{\text{physics}}$  to derive  $\mathbf{R}$  in Galerkin approach.



Similarly, the forward-backward propagation loop between  $\mathbf{a}$  and  $\tilde{\Pi}_{temp}$  can also be constructed by Ritz approach to derive the residual tensor of the next update step  $\mathbf{R}$  in line 10 of Algorithm 2, and between  $\mathbf{p}$  and  $\mathbf{p}^T \mathbf{K} \mathbf{p}$  to derive  $\mathbf{K} \mathbf{p}$  in line 9 of Algorithm 3. Besides, we can also choose Galerkin approach to operate on  $\mathbf{a}$ ,  $\mathbf{p}$  to derive  $\mathbf{R}$  and  $\mathbf{K} \mathbf{p}$ . For efficiency, we always use Galerkin approach to calculate matrix-vector products. Then the same mask operation is also imposed on  $\mathbf{R}$  and  $\mathbf{K} \mathbf{p}$  respectively.

With the update of current prediction  $\Delta \mathbf{a}_j^{bs}$ , we can manage to update the parameter  $\vartheta$  of the neural operator module. Here, we adopt a simple way to derive the update of  $\vartheta$ . First, we assume  $\mathbf{a}_j^{bs} + \Delta \mathbf{a}_j^{bs}$  to be a "provisional label" of the current batch. Then, we can define the loss metric that corresponds to the provisional label  $\hat{\mathbf{a}}_j^{bs} = \mathbf{a}_j^{bs} + \Delta \mathbf{a}_j^{bs}$  and the current prediction  $\mathbf{a}_j^{bs}$ , and we choose to use sum of squares error (SSE) as the loss metric:

$$\mathcal{L}_{SSE} = \frac{1}{2} \text{sum} \left( \text{square} \left( \hat{\mathbf{a}}_j^{bs} - \mathbf{a}_j^{bs} \right) \right) \quad (45)$$

Then in line 9 of Algorithm 1, The gradient of  $\vartheta$  is calculated with the chain rule<sup>1</sup>, which is easy to implement with Function class in `torch.autograd` module in Pytorch [36], then, the update of  $\vartheta$  is calculated with  $Opt_{net}$

$$\begin{aligned} \vartheta &= \vartheta - \hat{\eta} \cdot Opt_{net} \left( \text{einsum} \left( ' \dots t, \dots \rightarrow t', \text{grad} \left( \mathbf{a}_j^{bs}, \vartheta \right), \text{grad} \left( \mathcal{L}_{SSE}, \mathbf{a}_j^{bs} \right) \right) \right) \\ &= \vartheta + \hat{\eta} \cdot Opt_{net} \left( \text{einsum} \left( ' \dots t, \dots \rightarrow t', \text{grad} \left( \mathbf{a}_j^{bs}, \vartheta \right), \Delta \mathbf{a}_j^{bs} \right) \right) \end{aligned} \quad (46)$$

---

#### Algorithm 2 Steepest descent ( $n$ steps)

---

**Input:** residual tensor  $\mathbf{R}$ , current node solution  $\mathbf{a}$ , input parameter  $\mathbf{U}$ , mask operation  $Mask$

- 1:  $\mathbf{R} = -\mathbf{R}$
- 2:  $\Delta \mathbf{a} = \mathbf{0}$
- 3: **for**  $1 \leq i \leq n$  **do**
- 4:   Calculate  $\mathbf{R}^T \mathbf{K} \mathbf{R}$  corresponding to  $(\mathbf{U}, \mathbf{R})$
- 5:    $\alpha = \frac{\mathbf{R}^T \mathbf{R}}{\mathbf{R}^T \mathbf{K} \mathbf{R}}$
- 6:    $\Delta \mathbf{a} += \alpha \mathbf{R}$
- 7:   **if**  $n > 1$  **then**
- 8:      $\mathbf{a} += \alpha \mathbf{R}$
- 9:     Get  $\mathbf{R}$  with Ritz approach or Galerkin approach
- 10:     $\mathbf{R} = Mask(\mathbf{R})$
- 11:     $\mathbf{R} = -\mathbf{R}$
- 12:    **end if**
- 13: **end for**

**Return:**  $\Delta \mathbf{a}$

---

<sup>1</sup>For convenience, we consider the all trainable parameters  $\vartheta$  to form a vector.

---

**Algorithm 3 Conjugate gradient decent ( $n$  steps)**

---

**Input:** residual tensor  $\mathbf{R}$ , current node solution  $\mathbf{a}$ , input parameter  $\mathbf{U}$ , mask operation  $Mask$

```
1:  $\mathbf{R} = -\mathbf{R}$ 
2:  $\mathbf{p} = \mathbf{R}$ 
3:  $\Delta\mathbf{a} = \mathbf{0}$ 
4: for  $1 \leq i \leq n$  do
5:   Calculate  $\mathbf{p}^T \mathbf{K} \mathbf{p}$  corresponding to  $(\mathbf{U}, \mathbf{p})$ 
6:    $\alpha = \frac{\mathbf{R}^T \mathbf{R}}{\mathbf{p}^T \mathbf{K} \mathbf{p}}$ 
7:    $\Delta\mathbf{a} += \alpha \mathbf{p}$ 
8:   if  $n > 1$  then
9:     Get  $\mathbf{K} \mathbf{p}$  with Ritz approach or Galerkin approach
10:     $\mathbf{K} \mathbf{p} = Mask(\mathbf{K} \mathbf{p})$ 
11:     $\mathbf{R}_{new} = \mathbf{R} - \alpha \mathbf{K} \mathbf{p}$ 
12:     $\beta = \frac{\mathbf{R}_{new}^T \mathbf{R}_{new}}{\mathbf{R}^T \mathbf{R}}$ 
13:     $\mathbf{R} = \mathbf{R}_{new}$ 
14:     $\mathbf{p} = \mathbf{R} + \beta \mathbf{p}$ 
15:   end if
16: end for
Return:  $\Delta\mathbf{a}$ 
```

---

## 6 Conclusion and outlook

Both the conventional solver and the data-driven surrogate modeling have their own merits and shortcomings. The conventional solvers, which are based on the domain knowledge, can give reliable solutions to a wide variety of PDEs, and the conventional solvers are affordable when dealing with a single instance of PDEs or small number of samples, but they often have low efficiency and bring a heavy computational burden when the mass sampling of parameters of PDEs is required, because they usually only solve a single parameter each time. On the contrary, the data-driven surrogate modeling can give reasonable prediction of solutions to a range of parameters at a fast inference speed. However, as mentioned in Introduction (see section 1), the data-driven surrogate modeling needs a data preparation stage and a model training stage, which are isolated from each other. Besides, the access to substantial labeled data brings also quite a computational burden to the data-driven surrogate modeling. In machine learning field, more efficient training and less use of labels mean lower carbon, lower dataset costs and shorter experimental cycles. In this work, a novel data-efficient paradigm that has the merits of both and complements the shortcomings has been proposed, which we refer to as the variational operator learning (VOL). Our proposed VOL is part of an important effort to reduce the carbon footprint of research in the field of machine learning for PDEs and the numerical simulation. The proposed VOL achieves matrix-free approximation of system functional and residual with Ritz and Galerkin approaches. Direct residual minimization and iterative update, as two optimization strategies, are then proposed in VOL to learn PDEs' solution operators with a label-free training set. We have conducted various experiments on the variable heat source problem, the Darcy flow problem, and variable stiffness elasticity problem with two cases to demonstrate the effectiveness of VOL. Scaling experiments show test errors of VOL also follows a power law like LLMs [23, 34], and is able to learn solution operators with satisfactory results provided with enough cheap unlabeled data. Resolution experiments show VOL can learn solution operators largely efficiently when the solution field is discretized at different resolutions. We then design comparative experiments to verify generalization benefits of VOL, where we observe VOL has more superiority than classical iteration methods as the resolution increases. However, we also observe that, compared to classical iterative methods, the convergence speed is not significantly improved by the current

VOL algorithm, and the test errors of VOL have little improvement with larger number of update steps. Though we focus on training a neural operator module with iterative updates for the real-time inference, rather than accelerating the iterative solvers in the current work, it is still necessary to utilize techniques like preconditioners [2], multigrid methods [49], neural-accelerated solvers [45, 5], etc., to accelerate iterations. We then conduct comparative experiments for optimization strategies of VOL and the conventional data-driven strategy, results show the smaller residual norm does not refer to a smaller test error. While VOL achieves a smaller residual norm, it has a slightly larger test error than the data-driven strategy with the same training settings.

There are several aspects to be explored for the proposed VOL in the future work. Although VOL shows promise for label-free training of neural operators, it uses standard convolution operations, which limits its application on solution domains of arbitrary shapes. Graph operations and meshless methods will be considered in our future work to enhance the flexibility of the proposed VOL to handle solution domains with arbitrary shapes. In this Article, we mainly consider heat transfer, Darcy flow and elasticity physics at their steady-state cases, and in the future work, we will consider VOL on more complex physics phenomena, such as fluid dynamics, electromagnetics, and quantum mechanics. More iteration techniques and neural architectures will also be considered in VOL, such as generalized minimum residual method [40], multigrid algorithms [49, 51], factorized Fourier neural operators [48] and geometry-informed neural operators [30].

## 7 Acknowledgments

This work was supported by National Key Research and Development Program of China (2021YFF0306404), and National Natural Science Foundation of China (U21A20429 and U11772078).

## 8 Author contributions

T.X. and P.H. contributed to the original idea and design of the research. T.X. and D.L generated the datasets. T.X were responsible for software, data curation and formal analysis. P.H. acquired funding, and was responsible for the administration, resources and supervision of the project. All authors wrote, reviewed and edited the manuscript.

## References

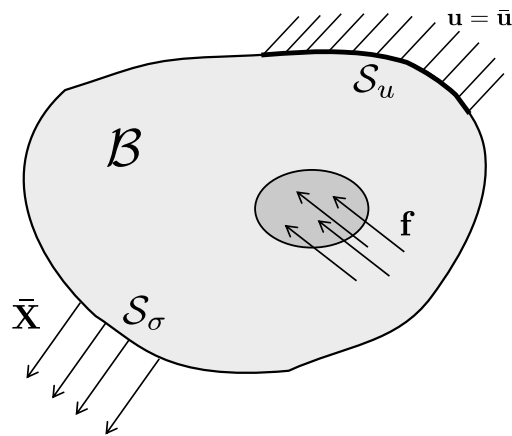
- [1] Kaushik Bhattacharya, Bamdad Hosseini, Nikola B. Kovachki, and Andrew M. Stuart. Model reduction and neural networks for parametric pdes. *The SMAI journal of computational mathematics*, 7:121–157, 07 2021.
- [2] Ke Chen. *Matrix preconditioning techniques and applications*. Cambridge University Press, 2005.
- [3] Tianping Chen and Hong Chen. Approximation capability to functions of several variables, nonlinear functionals, and operators by radial basis function neural networks. *IEEE Transactions on Neural Networks*, 6(4):904–910, 1995.
- [4] Tianping Chen and Hong Chen. Universal approximation to nonlinear operators by neural networks with arbitrary activation functions and its application to dynamical systems. *IEEE Transactions on Neural Networks*, 6(4):911–917, 1995.
- [5] Yuyan Chen, Bin Dong, and Jinchao Xu. Meta-mgnet: Meta multigrid networks for solving parameterized partial differential equations. *Journal of Computational Physics*, 455:110996, 2022.

- [6] Chen Cui, Kai Jiang, Yun Liu, and Shi Shu. Fourier neural solver for large sparse linear algebraic systems. *arXiv preprint arXiv:2210.03881*, 10 2022.
- [7] Weinan E and Bing Yu. The deep Ritz method: A deep learning-based numerical algorithm for solving variational problems. *Communications in Mathematics and Statistics*, 6:1–12, 3 2018.
- [8] Michael Eldred, Anthony Giunta, and S Collis. Second-order corrections for surrogate-based optimization with model hierarchies. In *10th AIAA/ISSMO multidisciplinary analysis and optimization conference*, page 4457, 2004.
- [9] Han Gao, Luning Sun, and Jian Xun Wang. PhyGeoNet: Physics-informed geometry-adaptive convolutional neural networks for solving parameterized steady-state pdes on irregular domain. *Journal of Computational Physics*, 428, 3 2021.
- [10] Somdatta Goswami, Katiana Kontolati, Michael D Shields, and George Em Karniadakis. Deep transfer operator learning for partial differential equations under conditional shift. *Nature Machine Intelligence*, 4:1155–1164, 12 2022.
- [11] Somdatta Goswami, Minglang Yin, Yue Yu, and George Em Karniadakis. A physics-informed variational deeponet for predicting crack path in quasi-brittle materials. *Computer Methods in Applied Mechanics and Engineering*, 391:114587, 2022.
- [12] Zafer Gürdal and Reynaldo Olmedo. In-plane response of laminates with spatially varying fiber orientations: Variable stiffness concept. *AIAA Journal*, 31:751–758, 1993.
- [13] Zafer Gürdal, Brian. F. Tatting, and C. K. Wu. Variable stiffness composite panels: Effects of stiffness variation on the in-plane and buckling response. *Composites Part A: Applied Science and Manufacturing*, 39:911–922, 5 2008.
- [14] Jiequn Han, Linfeng Zhang, Roberto Car, and Weinan E. Deep Potential: A general representation of a many-body potential energy surface. *Communications in Computational Physics*, 23, 2018.
- [15] Zhongkai Hao, Chengyang Ying, Zhengyi Wang, Hang Su, Yinpeng Dong, Songming Liu, Ze Cheng, Jun Zhu, and Jian Song. GNOT: A general neural operator transformer for operator learning. *arXiv preprint arXiv:2302.14376*, 2023.
- [16] Juncai He and Jinchao Xu. MgNet: A unified framework of multigrid and convolutional neural network. *Science China Mathematics*, 62:1331–1354, 05 2019.
- [17] Jan S Hesthaven, Gianluigi Rozza, Benjamin Stamm, et al. *Certified reduced basis methods for parametrized partial differential equations*, volume 590. Springer, 2016.
- [18] Mengcheng Huang, Zongliang Du, Chang Liu, Yonggang Zheng, Tianchen Cui, Yue Mei, Xiao Li, Xiaoyu Zhang, and Xu Guo. Problem-independent machine learning (PIML)-based topology optimization—a universal approach. *Extreme Mechanics Letters*, 56, 10 2022.
- [19] Xiang Huang, Zhanhong Ye, Hongsheng Liu, Bei Shi, Zidong Wang, Kang Yang, Yan Li, Bingya Weng, Min Wang, Haotian Chu, Jing Zhou, Fan Yu, Bei Hua, Lei Chen, and Bin Dong. Meta-auto-decoder for solving parametric partial differential equations. *arXiv preprint arXiv:2111.08823*, 11 2021.
- [20] Haoliang Jiang, Zhenguang Nie, Roselyn Yeo, Amir Barati Farimani, and Levent Burak Kara. StressGAN: A generative deep learning model for two-dimensional stress distribution prediction. *Journal of Applied Mechanics, Transactions ASME*, 88, 5 2021.

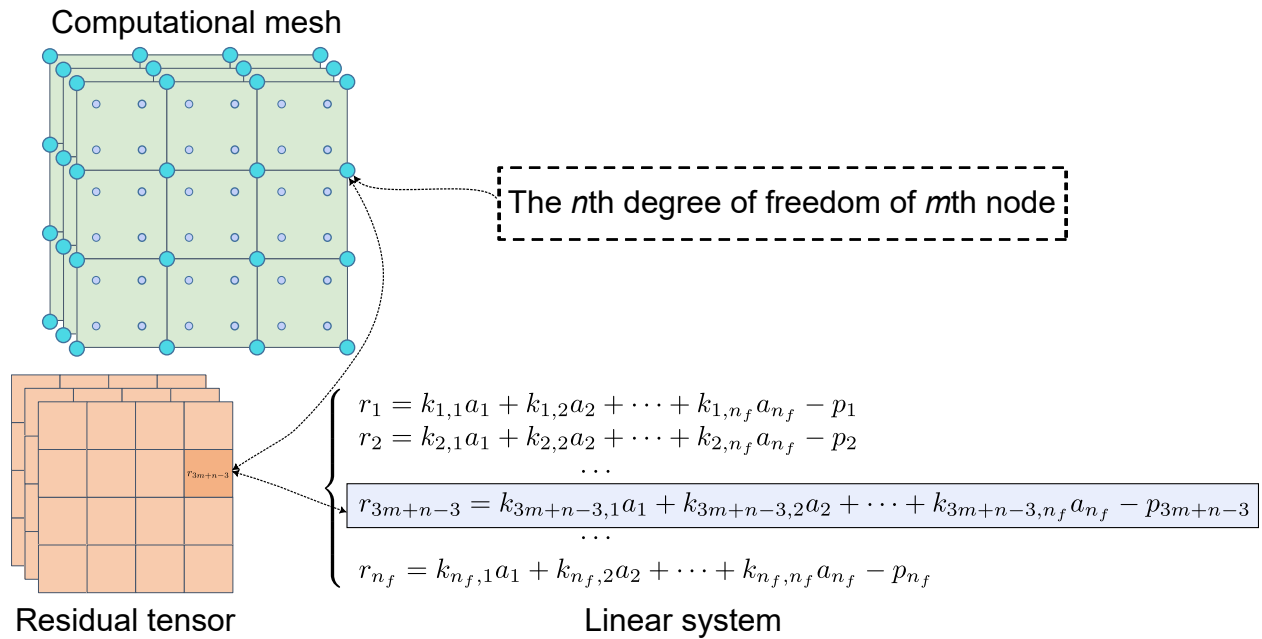
- [21] Pengzhan Jin, Shuai Meng, and Lu Lu. Mionet: Learning multiple-input operators via tensor product. *SIAM Journal on Scientific Computing*, 44(6):A3490–A3514, 2022.
- [22] Ayano Kaneda, Osman Akar, Jingyu Chen, Victoria Kala, David Hyde, and Joseph Teran. A deep conjugate direction method for iteratively solving linear systems. *arXiv preprint arXiv:2205.10763*, 5 2022.
- [23] Jared Kaplan, Sam McCandlish, Tom Henighan, Tom B. Brown, Benjamin Chess, Rewon Child, Scott Gray, Alec Radford, Jeffrey Wu, and Dario Amodei. Scaling laws for neural language models. *arXiv preprint arXiv:2001.08361*, 2020.
- [24] Reza Khodayi-Mehr and Michael Zavlanos. VarNet: Variational neural networks for the solution of partial differential equations. In *Proceedings of the 2nd Conference on Learning for Dynamics and Control*, volume 120 of *Proceedings of Machine Learning Research*, pages 298–307. PMLR, 10–11 Jun 2020.
- [25] Georgios Kissas, J S Seidman, Leonardo Ferreira Guilhoto, Víctor M Preciado, George J Pappas, and Paris Perdikaris. Learning operators with coupled attention. *arXiv preprint arXiv:2201.01032*, 2022.
- [26] Alex Krizhevsky and Geoffrey E. Hinton. Learning multiple layers of features from tiny images. Technical report, Department of Computer Science, University of Toronto, 2009.
- [27] Samuel Lanthaler. Operator learning with pca-net: upper and lower complexity bounds. *arXiv preprint arXiv:2303.16317*, 2023.
- [28] Zongyi Li, Nikola Kovachki, Kamyar Azizzadenesheli, Burigede Liu, Kaushik Bhattacharya, Andrew Stuart, and Anima Anandkumar. Fourier neural operator for parametric partial differential equations. *arXiv preprint arXiv:2010.08895*, 2020.
- [29] Zongyi Li, Nikola B Kovachki, Kamyar Azizzadenesheli, Burigede Liu, Kaushik Bhattacharya, Andrew M Stuart, and Anima Anandkumar. Neural operator: Graph kernel network for partial differential equations. In *International Conference on Learning Representations*, 2020.
- [30] Zongyi Li, Nikola Borislavov Kovachki, Chris Choy, Boyi Li, Jean Kossaifi, Shourya Prakash Otta, Mohammad Amin Nabian, Maximilian Stadler, Christian Hundt, Kamyar Azizzadenesheli, and Anima Anandkumar. Geometry-informed neural operator for large-scale 3d pdes. *arXiv preprint arXiv:2309.00583*, 2023.
- [31] Zongyi Li, Hongkai Zheng, Nikola Kovachki, David Jin, Haoxuan Chen, Burigede Liu, Kamyar Azizzadenesheli, and Anima Anandkumar. Physics-informed neural operator for learning partial differential equations. *arXiv preprint arXiv:2111.03794*, 11 2021.
- [32] Lu Lu, Pengzhan Jin, Guofei Pang, Zhongqiang Zhang, and George Em Karniadakis. Learning nonlinear operators via DeepONet based on the universal approximation theorem of operators. *Nature Machine Intelligence*, 3:218–229, 3 2021.
- [33] Lu Lu, Xuhui Meng, Shengze Cai, Zhiping Mao, Somdatta Goswami, Zhongqiang Zhang, and George Em Karniadakis. A comprehensive and fair comparison of two neural operators (with practical extensions) based on fair data. *Computer Methods in Applied Mechanics and Engineering*, 393:114778, 04 2022.
- [34] Alexander Maloney, Daniel A Roberts, and James Sully. A solvable model of neural scaling laws. *arXiv preprint arXiv:2210.16859*, 2022.

- [35] Zhenguo Nie, Haoliang Jiang, and Levent Burak Kara. Stress field prediction in cantilevered structures using convolutional neural networks. *Journal of Computing and Information Science in Engineering*, 20, 2 2020.
- [36] Adam Paszke, Sam Gross, Francisco Massa, Adam Lerer, James Bradbury, Gregory Chanan, Trevor Killeen, Zeming Lin, Natalia Gimelshein, Luca Antiga, Alban Desmaison, Andreas Kopf, Edward Yang, Zachary DeVito, Martin Raison, Alykhan Tejani, Sasank Chilamkurthy, Benoit Steiner, Lu Fang, Junjie Bai, and Soumith Chintala. PyTorch: An imperative style, high-performance deep learning library. In *Advances in Neural Information Processing Systems 32*, pages 8024–8035. Curran Associates, Inc., 2019.
- [37] Maziar Raissi, Paris Perdikaris, and George Em Karniadakis. Physics-informed neural networks: A deep learning framework for solving forward and inverse problems involving nonlinear partial differential equations. *Journal of Computational Physics*, 378:686–707, 02 2019.
- [38] Rishikesh Ranade, Chris Hill, and Jay Pathak. DiscretizationNet: A machine-learning based solver for navier–stokes equations using finite volume discretization. *Computer Methods in Applied Mechanics and Engineering*, 378, 5 2021.
- [39] Chengping Rao, Pu Ren, Qi Wang, Oral Buyukozturk, Hao Sun, and Yang Liu. Encoding physics to learn reaction–diffusion processes. *Nature Machine Intelligence*, 5:765–779, 07 2023.
- [40] Y Saad. *Iterative methods for sparse linear systems*. Siam, 2003.
- [41] E. Samaniego, C. Anitescu, S. Goswami, V.M. Nguyen-Thanh, H. Guo, K. Hamdia, X. Zhuang, and T. Rabczuk. An energy approach to the solution of partial differential equations in computational mechanics via machine learning: Concepts, implementation and applications. *Computer Methods in Applied Mechanics and Engineering*, 362:112790, 04 2020.
- [42] Jacob Seidman, Georgios Kissas, Paris Perdikaris, and George J. Pappas. Nomad: Nonlinear manifold decoders for operator learning. In S. Koyejo, S. Mohamed, A. Agarwal, D. Belgrave, K. Cho, and A. Oh, editors, *Advances in Neural Information Processing Systems*, volume 35, pages 5601–5613. Curran Associates, Inc., 2022.
- [43] Burr Settles. Active learning literature survey. Computer Sciences Technical Report 1648, University of Wisconsin–Madison, 2009.
- [44] Justin Sirignano and Konstantinos Spiliopoulos. DGM: A deep learning algorithm for solving partial differential equations. *Journal of Computational Physics*, 375:1339–1364, 12 2018.
- [45] Antonio Stanzola, Simon R. Arridge, Ben T. Cox, and Bradley E. Treeby. A helmholtz equation solver using unsupervised learning: Application to transcranial ultrasound. *Journal of Computational Physics*, page 110430, 2021.
- [46] N. Sukumar and Ankit Srivastava. Exact imposition of boundary conditions with distance functions in physics-informed deep neural networks. *Computer Methods in Applied Mechanics and Engineering*, 389:114333, 2022.
- [47] Luning Sun, Han Gao, Shaowu Pan, and Jian-Xun Wang. Surrogate modeling for fluid flows based on physics-constrained deep learning without simulation data. *Computer Methods in Applied Mechanics and Engineering*, 361:112732, 04 2020.

- [48] Alasdair Tran, Alexander Mathews, Lexing Xie, and Cheng Soon Ong. Factorized fourier neural operators. In *The Eleventh International Conference on Learning Representations*, 2023.
- [49] Ulrich Trottenberg, A Brandt, Cornelis W Oosterlee, P Oswald, Anton Schüller, and K Stüben. *Multi-grid*. Elsevier/Academic Press, 2001.
- [50] Sifan Wang, Hanwen Wang, and Paris Perdikaris. Learning the solution operator of parametric partial differential equations with physics-informed DeepONets. *Science Advances*, 7, 10 2021.
- [51] Jinchao Xu and Ludmil Zikatanov. Algebraic multigrid methods. *Acta Numerica*, 26:591–721, 05 2017.
- [52] Houpu Yao, Yi Gao, and Yongming Liu. FEA-Net: A physics-guided data-driven model for efficient mechanical response prediction. *Computer Methods in Applied Mechanics and Engineering*, 363:112892, 5 2020.
- [53] Huaiqian You, Quinn Zhang, Colton J. Ross, Chung-Hao Lee, and Yue Yu. Learning deep implicit fourier neural operators (IFNOs) with applications to heterogeneous material modeling. *Computer Methods in Applied Mechanics and Engineering*, 398:115296, 08 2022.
- [54] Hong Wu Zhang, Jing Kai Wu, Jun Lü, and Zhen Dong Fu. Extended multiscale finite element method for mechanical analysis of heterogeneous materials. *Acta Mechanica Sinica/Lixue Xuebao*, 26:899–920, 12 2010.
- [55] Kunpeng Zhang, Dachuan Liu, Qun Wang, Peng Hao, Yuhui Duan, Hao Tang, and Bo Wang. Multi-level intelligent design of variable angle tow laminates via image-driven method. *Composite Structures*, 303, 1 2023.

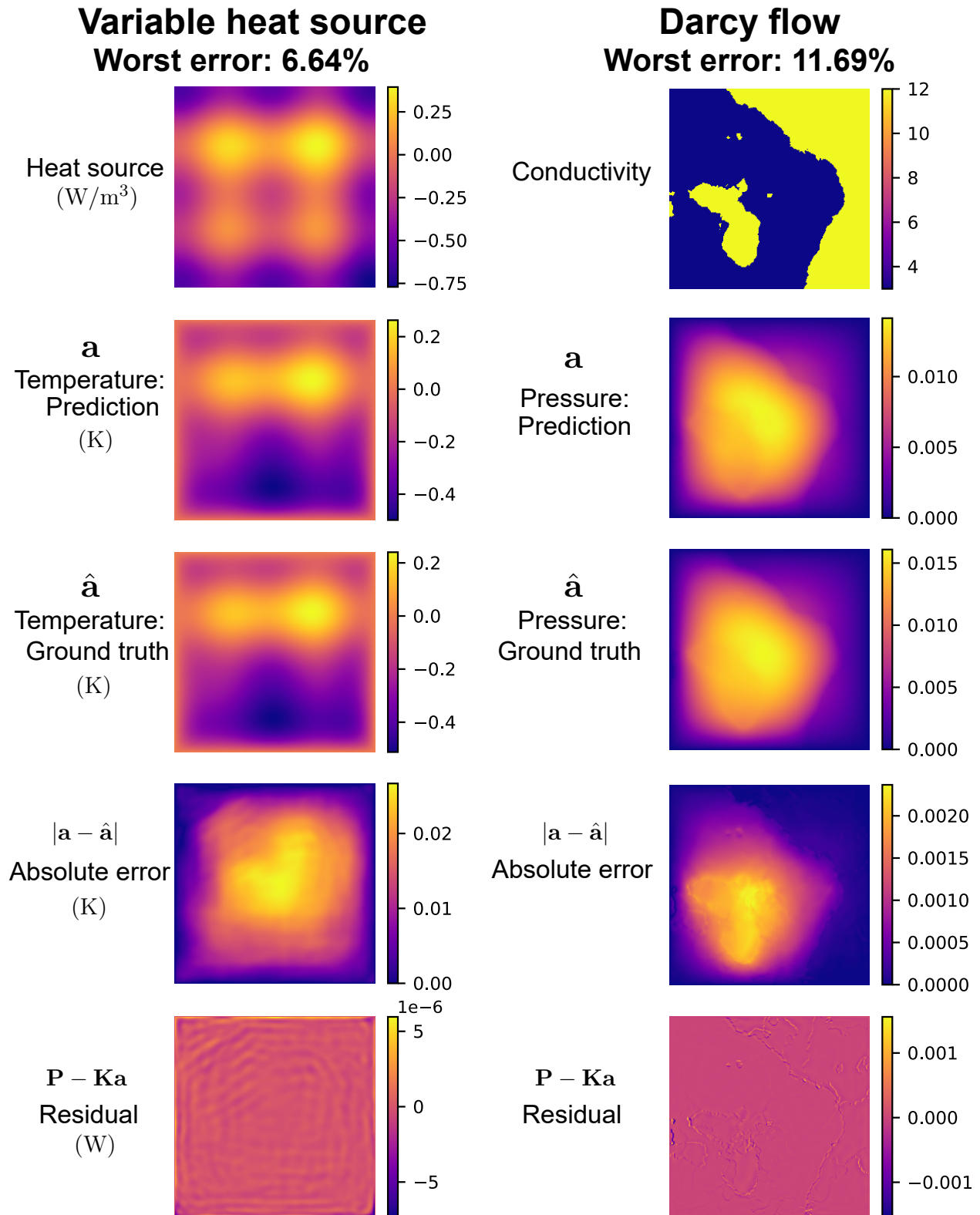


Extended Data Figure 1: A linear elastic body with body forces and boundary conditions.



Extended Data Figure 2: **The relationship between the computational mesh, the residual tensor and the linear system.** Suppose that every node of the computational mesh has three degrees of freedom. The element  $r_{3m+n-3}$  of the residual tensor is just the residual of the  $(3m + n - 3)$ th equation of the corresponding linear system.

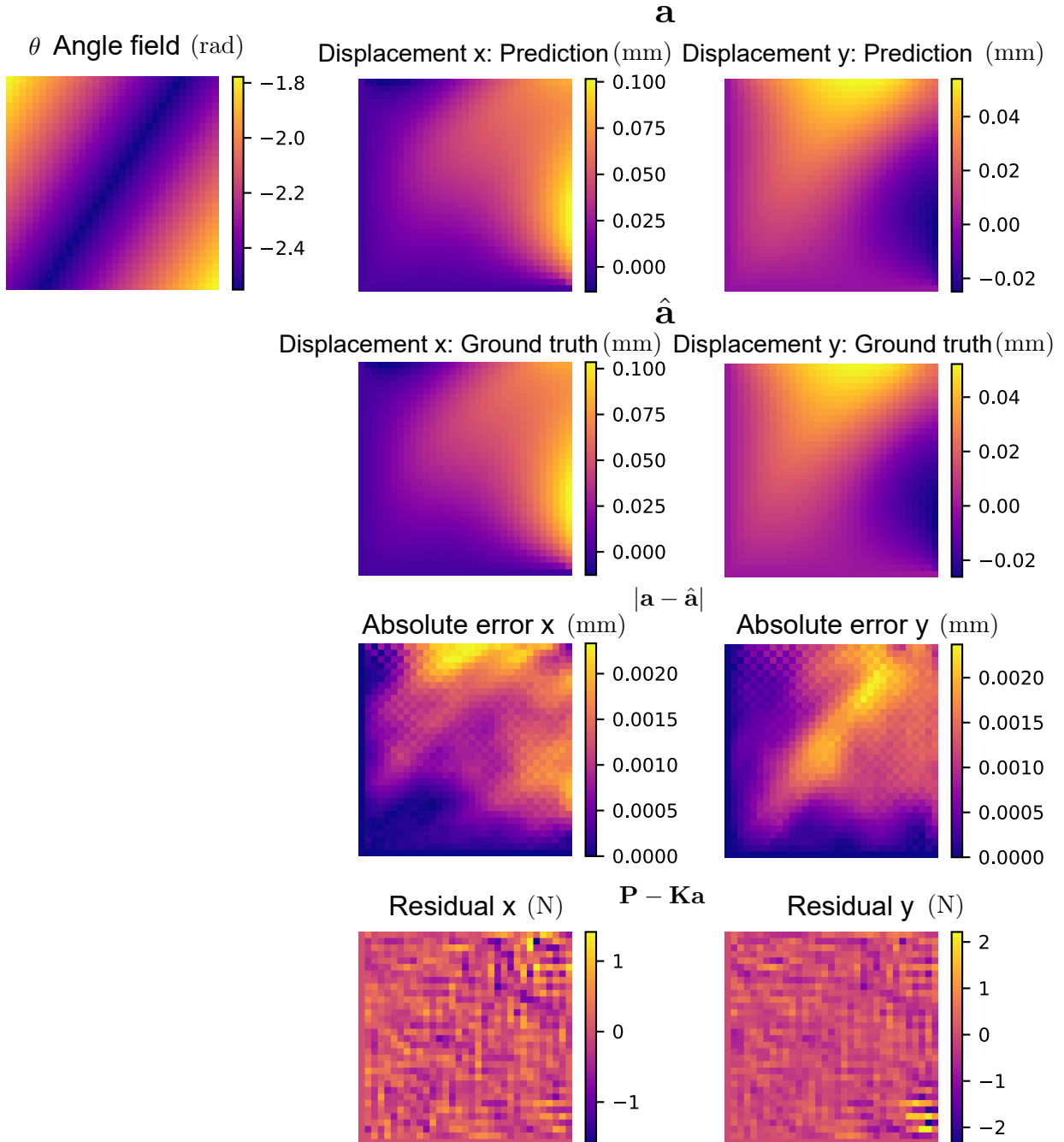




Extended Data Figure 3: **Worst samples of variable heat source problem and darcy problem in scaling experiments.** ( $N_{\text{training set}} = 10000$ ,  $N_{\text{test set}} = 2000$ ).

## Elasticity A

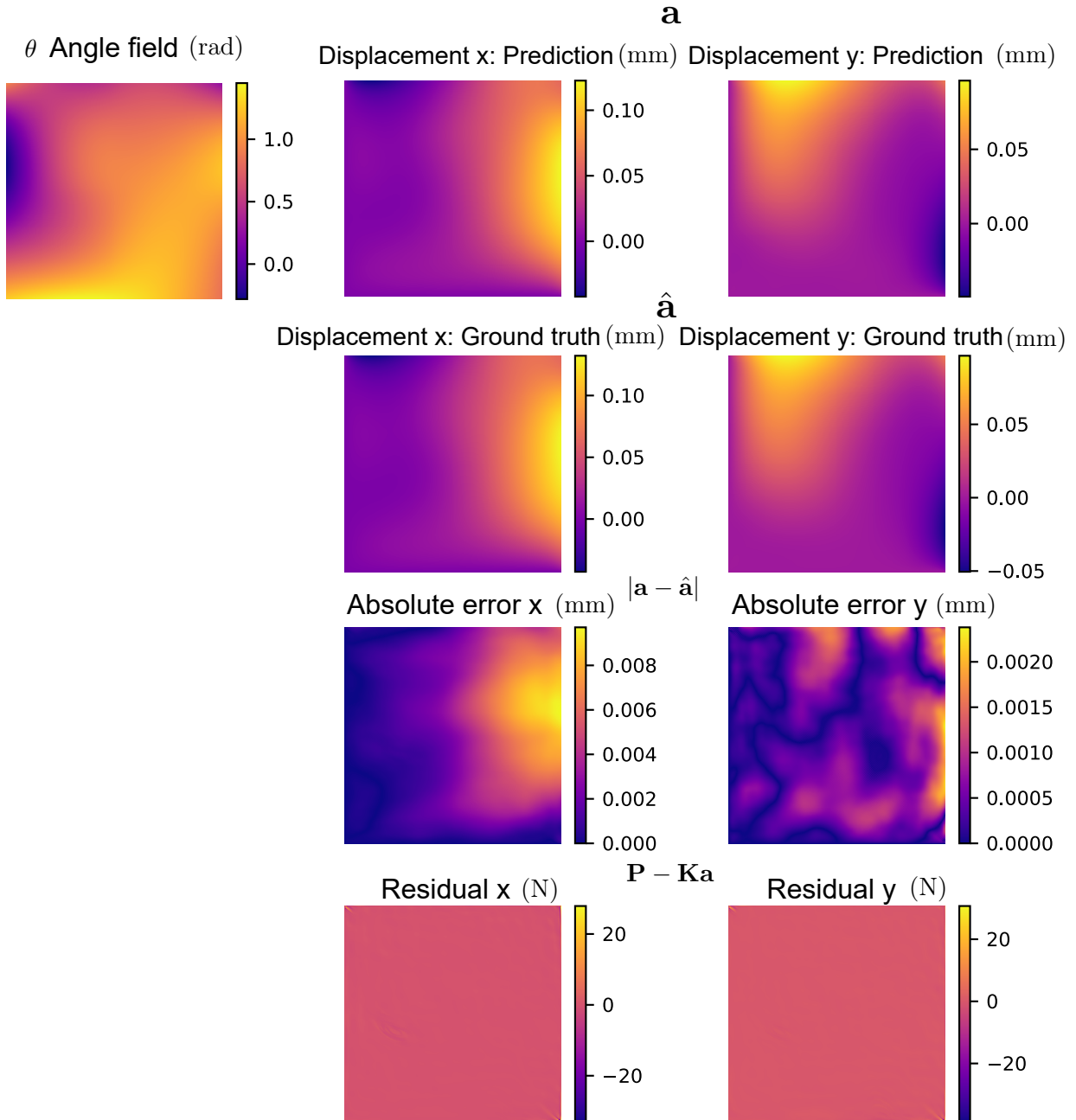
**Worst error: 3.33%**



Extended Data Figure 4: **Worst samples of elasticity A problem in scaling experiments.** ( $N_{\text{training set}} = 10000$ ,  $N_{\text{test set}} = 2000$ ).

## Elasticity B

**Worst error: 7.14%**



Extended Data Figure 5: **Worst samples of elasticity B problem in scaling experiments.** ( $N_{\text{training set}} = 10000$ ,  $N_{\text{test set}} = 2000$ ).